A STUDY OF STRAINED InGaAs-AlGaAs MQW STRUCTURES GROWN ON (111)B GaAs SUBSTRATES

By

ZIAD OSMAN

A DISSERTATION PRESENTED TO THE GRADUATE SCHOOL
OF THE UNIVERSITY OF FLORIDA IN PARTIAL FULFILLEMENT
OF THE REQUIREMENTS FOR THE DEGREE OF
DOCTOR OF PHILOSOPHY

UNIVERSITY OF FLORIDA

1994

IN THE NAME OF ALLAH MOST GRACIOUS MOST MERCIFUL

Read in the name of thy Lord and Cherisher who created.

Created man, out of mere clot of congealed blood.

Read! And thy Lord is most Bountiful.

He who taught the use of the Pen.

Taught man that which he knew not.

Surah 96, Verses 1-5
The Translation of the Meaning
of the First Revealed
of the Holy Qur'an

ACKNOWLEDGMENTS

I want, first and foremost, to thank Allah for all the bounties He gave me, where the completion of this dissertation is one of them. I would like to express my gratitude to Dr. Utpal Das for his enlightening guidance and for his endless support throughout this work. I wish to extend my appreciation to all my committee members for their helpful insights especially Dr. Ramakant Srivastava, whose support and supervision helped me through the last stages of this project. I would also want to thank my colleague Muthu for all the help that he provided during the course of this research. I am deeply indebted to my family and to my fiancee for their constant support and encouragement.

TABLE OF CONTENTS

ACKNOWLEDGEMENTS iii

ABSTRACT vi

CHAPTER 1 INTRODUCTION 1

CHAPTER 2 FILM GROWTH ON (111)B GaAs 4

2.1 Introduction 4
2.2 Growth on (111) Oriented Substrates 4
2.2.1 Introduction 4
2.2.2 Molecular Beam Epitaxy(MBE)Growth 5
2.2.3 Growth of GaAs, AlGaAs, and InGaAs 8

CHAPTER 3 CHARACTERISTICS OF STRAINED MQW STRUCTURES GROWN ON (111)B GaAs SUBSTRATES 18

3.1 Introduction 18
3.2 Characteristics of Strained Structures on (111)B Substrates 19
3.2.1 Effective Mass Changes due to the Growth Orientation 19
3.2.2 Piezoelectric Effect 21
3.2.3 Band Structure Modification due to Strain Effect 26
3.3 A Study of (111)B Grown Strained MQW Structures 27
3.3.1 Introduction 27
3.3.2 Kronig-Penney Model 30
3.3.3 Strain Effect on C1-HH1 Transition Energy 34
3.3.4 Electric Field Effect on QWs 35
3.3.5 Combined Effects 43
3.3.6 Advantages of the Proposed Structures . 43

CHAPTER 4 EFFECT OF OPTICAL EXCITATION AND MECHANICAL STRESS ON THE CHARACTERISTICS OF THE STRUCTURES 48

4.1 Introduction 48
4.2 Effect of Optical Excitation 49
4.3 PL Measurements 50
4.4 Amount of E-Field Screening 53
4.5 Mechanical Strain Effect 60

CHAPTER 5 CHARACTERIZATION OF THE THIRD ORDER NONLINEARITY 70

5.1 Introduction 70
5.2 Waveguiding Properties of the Structures 71
5.2.1 Multilayer Matrix Theory 71
5.2.2 Refractive Index of Different Layers .. 78
5.3 Nonlinearities in Proposed Structures 80
5.3.1 Introduction 80
5.3.2 Measurements of the Nonlinear Refractive Index 88

CHAPTER 6 CONCLUSIONS AND RECOMMENDATIONS 98

APPENDIX A CALCULATION OF THE C1-HH1&LH1 TRANSITION ENERGIES IN (100) SAMPLES 101

APPENDIX B CALCULATION OF THE C1-HH1&LH1 TRANSITION ENERGIES IN (111) SAMPLES 111

APPENDIX C CALCULATION OF THE REFRACTIVE INDICES FOR THE LAYERS IN STRUCTURES S1 AND S2 120

APPENDIX D CONDITIONS FOR SINGLE MODE OPERATION 124

REFERENCE LIST 140

BIOGRAPHICAL SKETCH 145

Abstract of Dissertation Presented to the Graduate School of the University of Florida in Partial Fulfillment of the Requirements for the Degree of Doctor of Philosophy

A STUDY OF STRAINED InGaAs-AlGaAs MQW STRUCTURES GROWN ON (111)B GaAs SUBSTRATES

By

Ziad Osman

August 1994

Chairperson: Ramakant Srivastava
Major Department: Electrical Engineering

The presence of strain-induced electric fields in lattice mismatched quantum wells (QWs) grown along the (111) growth axis gives these structures advantages over those grown along the (100) growth axis. The electric field shifts the excitonic resonance to lower energy (intrinsic Stark effect) and decreases the optical matrix element. This feature is absent in the case of (100) grown layers where the piezoelectricity along this axis does not produce any electric field.

In this work we present the theory used to estimate the strain-induced electric field present in (111) grown $In_xGa_{1-x}As/Al_{0.2}Ga_{0.8}As$ p-i-n structures for x = 5% and 10%. The presence of this field was proved by the use of intensity-dependent photoluminescence measurements, where an increase in the laser light intensity used in the PL would

subsequently increase the number of optically created e-h pairs in the wells, acting to screen the electric field, causing the shift of the excitonic transition energy to a higher value.

In an effort to further investigate the effect of the strain, a (111) grown sample was subjected to external mechanical tensile strain. This is done by placing the sample on a diaphragm that is allowed to move under the application of a bias, which produced a pulling force on the sample, i.e. tensile strain, causing a shift in the excitonic peak toward a lower transition energy. This study thus corroborated the existence of the built-in electric field in (111) grown samples.

Finally, the nonlinear refractive index for the samples grown on (111)B and (100) substrates was measured using a hybrid Mach-Zender interferometer setup, with a TE polarized laser light at two wavelengths (980 and 992.2 nm). An improvement in the figure of merit for the (111) grown layers, compared to those grown on (100), was observed. This finding makes the use of (111) grown structures as nonlinear devices more advantageous than the (100) ones.

CHAPTER 1
INTRODUCTION

The use of lattice mismatched material has been extensively studied for structures grown on (100) GaAs substrates for their use in optical and electrooptical devices (mainly having InGaAs/GaAs or AlGaAs MQW structure)[1-5]. More recently a new effect in strained-layer superlattices with a [111] growth axis has been predicted. It is the presence of a large internal electric field generated by the piezoelectric effect [6]. Group III-V semiconductors are piezoelectric; thus, strain in these materials can lead to electric polarization fields. The magnitude of these fields can be very large exceeding 10^5 V/cm for lattice constant mismatches of the order of 1% [6].

The strain generated electric field substantially changes the properties of (111) strained quantum wells and can lead to large nonlinear optic and electrooptic effects [7,8]. It causes the tilt of the energy bands and leads to a red shift of the optical transition energies [9,10].

In this dissertation we investigate the effects mentioned above for compressively strained InGaAs/AlGaAs MQW structures grown on (111)B (As terminated) GaAs substrates.

Chapter 2 explains film growth procedure on (111)B GaAs substrates using a Molecular Beam Epitaxy system. The growth of GaAs, AlGaAs and InGaAs is specially emphasized. We also present the advantages of the growth along this axis compared to (100).

Chapter 3 deals with the theory of the strain-induced electric field in strained MQWs structures, showing the main differences between (100) and (111) grown structures. Then, two structures with 5% and 10% In concentrations are presented. The Kronig-Penney model is introduced in order to estimate the value of the C1-HH1 transition energies in the samples, keeping in mind the presence of the electric field in the (111) grown samples, causing the transition energy in the wells to shift to lower energies. This effect is interpreted using an effective well width model proposed by Miller et al. [11].

Chapter 4 discusses the effect of the increase of optical excitation on the C1-HH1 transition energy. The production of electron-hole pairs in large numbers tends to create an electric field which screens the built-in electric field, and in turn shifting the transition energy toward a higher energy value only in the (111) grown structures. This is proven by the use of a low temperature photoluminescence setup. Furthermore, the effect that an externally applied strain has on a (111) grown structure is measured by monitoring the induced energy shift. A simulation is run to

determine the expected change in the layer mismatch and therefore the electric field.

Chapter 5 presents the means used to measure the value of the nonlinear refractive index in all the structures. It is important to make sure that the compositions, i.e. refractive indices of the layers constituting the structures would act as single mode slab waveguides at the wavelengths of interest. The single effective oscillator (SEO) and the multilayer matrix method are used to determine the refractive indices, and to insure a single lateral mode operation, respectively. Then, a hybrid Mach-Zender setup is used to obtain the values of n_2 for the different samples, showing the advantage that (111) grown samples have over (100) ones.

Finally, Chapter 6 summarizes the work we have undertaken in the course of this research, giving some predictions and recommendations for further studies.

CHAPTER 2
FILM GROWTH ON (111)B GaAs

2.1 Introduction

III-V compound semiconductors have been grown traditionally on (100) substrates because of the wide range of growth conditions which result in good epitaxial layer quality on the this crystalline orientation. However, fundamental material properties, growth mechanisms, surface kinetics, and quantum well properties can be changed or improved as compared to those on (100)[9,12,13]. It has been theoretically predicted and observed that coherently strained (110) and (111) layers will possess a large built-in in-plane or perpendicular-to-plane piezoelectric field, which leads to a new class of self electro-optic devices. Quantum wells grown on (111) possess an enhanced optical transition [14], and a low-threshold (111) QW laser has been made [12].

2.2 Growth on (111) Oriented Substrates

2.2.1 Introduction

It is rather difficult to grow high quality materials on (111) substrates [15]. Either forced two-dimensional

layer-by-layer migration enhanced epitaxy or a very high growth temperature (700°C) are required to suppress microtwins and facet growth on (111). However, Chin et al.[16-18] were able to grow high quality layers of GaAs, AlGaAs and InGaAs on (111)B GaAs.

To achieve this goal, Chin et al.[16-18] have examined a variety of miscuts on (111)B GaAs. Few degrees of miscut can provide growth ledges to achieve two-dimensional step flow epitaxy. It was found that if (111)B was miscut toward <211> instead of <100> and <011>, a wide range of angles (1°-3°) can generate a smooth growth. Although it was also found that 0.5° miscut toward <100> can achieve a very high quality material [12], it was not used in the growth of the proposed structures because an exact 0.5° miscut is extremely difficult to control. A proper choice of miscut is the key in achieving a high quality material on (111), over a wide range of growth conditions. To discover which of the miscut angles is best for growth, GaAs and AlGaAs were grown on (111)B GaAs.

2.2.2 Molecular Beam Epitaxy (MBE) Growth

The essential elements of a MBE system [19] are shown in Fig. 2.1. It is apparent from this illustration that each MBE arrangement may be divided into three zones where three different physical phenomena take place [20]. The first zone is the generation zone of the molecular beams. Next is the

zone where the beams from different sources intersect each other and the vaporized elements mix together creating a very special gas phase contacting the substrate area. This area, where the crystallization processes take place, can be regarded as the third zone of the MBE physical system.

The molecular beams are generated in the first zone under UHV conditions from sources of the Knudsen-effusion-cell type [20], whose temperatures are accurately controlled. Conventional temperature control, based on high performance proportional-integral-derivative (PID) controllers and thermocouple feedback, enables a flux stability of better than ±1% [21]. By choosing appropriate cell and substrate temperatures, epitaxial films of the desired chemical composition can be obtained. Accurately selected and subsequently precisely controlled temperatures of the substrates and each of the sources of the constituent beams have thus a different effect upon the growth process.

The second zone in the MBE vacuum reactor is the mixing zone, where the molecular beams intersect each other. Little is known at present about the physical phenomena occurring in this zone. This results from the fact that usually the mean free path of the molecules belonging to the intersecting beams is so long that no collisions and no other interactions between the molecules of different species occur there.

Epitaxial growth in MBE is realized in the third zone, i.e. on the substrate surface. A series of surface processes is involved in MBE growth; however, the following are the

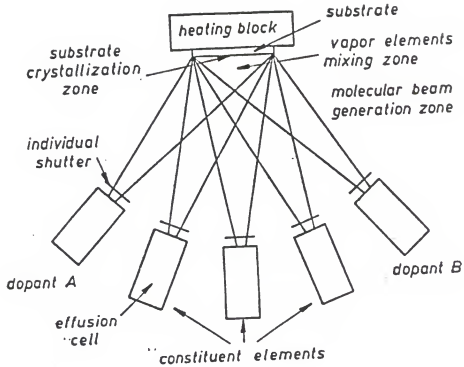

Fig 2.1 Schematic illustration of the essential parts of an MBE growth system [19].

most important [22] :

i) Adsorption of the constituent atoms or molecules impinging on the substrate surface.

ii) Surface migration and dissociation of the adsorbed molecules.

iii) Incorporation of the constituent atoms into the crystal lattice of the substrate or the epilayer already grown.

iv) Thermal desorption of the species not incorporated into the crystal lattice.

These processes are schematically illustrated in Fig 2.2 [23]. The substrate crystal surface is divided into so-called crystal sites on which the impinging molecules or atoms may interact. Each crystal part is a small part of the crystal surface characterized by its individual chemical activity. A site can be created by a dangling bond, vacancy, step edge, etc. [24].

2.2.3 Growth of GaAs, AlGaAs, and InGaAs

A Varian Modular GEN II Molecular Beam Epitaxial growth system was used to grow GaAs and AlGaAs on (111)B and (100) substrates simultaneously. This system was carefully baked and outgassed to reduce background impurities. After a few days of bakeout and cooling, the chamber pressure is lower than $1x10^{-11}$ Torr. The careful outgas procedure and low ambient pressures of CO, H_2O, and O_2 molecules are important to achieve high quality growth with low concentrations of

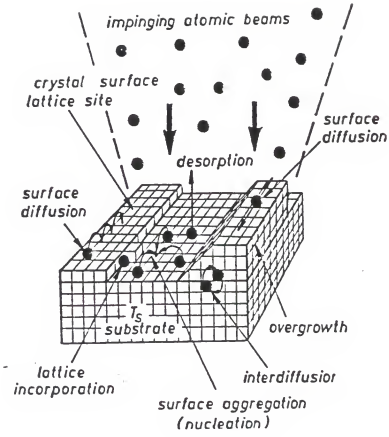

Fig 2.2 Schematic illustration of the surface processes occurring during film growth by MBE [22].

nonradiative recombination centers.

The quality of the grown material was characterized by the use of low temperature photoluminescence (PL) measurements. Chin et al.[12] found that the principal spectral features of the GaAs layer grown on (100) are neutral donor bound (D^o,X) and acceptor bound (A^o,X) exciton recombination lines and free electron-acceptor (e,A^o) and donor acceptor (D^o,A^o) transitions. However, only the neutral donor bound exciton transition was observed for the GaAs layer grown on (111)B.

The acceptor related transition for (100) is due to carbon incorporated into the GaAs layer from MBE background carbon-related species such as CO, CH_4, etc. The donor related transition is due to sulfur in high quality MBE grown GaAs.

Low carbon acceptor incorporation in (111)B GaAs can be understood based on the number of dangling bonds. While the (100) surface always has two double dangling bonds available for both Ga and As surface adatoms, the (111)B surface has either one or three dangling bonds available for Ga and As, respectively (see Fig. 2.3). The large number of dangling bonds available to As on (111)B increase the As sticking coefficient and reduce surface lifetime for As adatoms. Thus the probability for carbon incorporation is much reduced. This is one of the advantages of material growth on (111)B since low carbon incorporation in GaAs improves the material transport properties.

Next, Chin et al.[18], compared the growth of 2μm $Al_{0.22}Ga_{0.78}As$ on (100) and (111)B GaAs. Growth was carried out simultaneously on 1°, 2° and 3° misoriented (111)B and 0°(100) GaAs substrates at 630 and 670°C, respectively.

The PL spectra for the growth temperature of 630°C are shown in Fig. 2.4. A full width at half-maximum (FWHM) of 4.4 meV for (100) AlGaAs indicates excellent quality. The high energy peak at 1.837 eV is due to bound excitons. The broad peak centered at 1.818 eV is a combination of electron-to-neutral-carbon-acceptor and neutral-donor-to-neutral-acceptor recombination.

The (111)B AlGaAs layers show broad peaks without any resolvable fine structures. The peak energies decrease monotonically from 1.837 eV for 0°(100) to 1.744 eV for the 3°(111)B layer (a shift of 93 meV). The 1° and 3° misoriented layers show single peaks almost 10 times as intense as that of the (100), whereas the 2° misoriented layer shows two peaks half as intense as those of 1° and 3° misorientations. The fact that the PL spectra are not due to impurity related transitions is evidenced by low impurity content of the layers indicated by Hall mobility measurements. The FWHM for 1° and 3° misorientations, however, increases to 17.5 and 20.2 meV, respectively. The half-widths at half-maximum (HWHM) for 2° misorientation peaks are 9.5 and 20.2 meV.

Figure 2.5 shows the PL spectra of the AlGaAs grown at 670°C. The energy of the peak of the 0°(100) layer is about 8 meV higher than that grown at 630°C. This shift in energy is

due to higher Ga desorption (re-evaporation of surface Ga adatoms) at this growth temperature, with a slight increase in the linewidth to 5.0 meV. The peak intensities for (111)B show little change from that grown on 0°(100) substrate although a decrease in the linewidth is observed from a 16.4 meV for 1° to 8.8 meV for 3° misorientation. All the peak energies lie within 9 meV of that for the (100) layer and the maximum increase in the integrated intensity is by a factor of 2.7 only. The absence of any significant orientation dependence of the PL for the layers grown at 670°C is believed to be due to high surface migration of both Al and Ga adatoms.

The relative PL integrated intensity and peak energy shifts are summarized in Figs. 2.6a and 2.6b , respectively. An order of magnitude intensity enhancement in (100) AlGaAs grown at 670°C compared to 630°C is due to reduction in the defect related nonradiative recombination centers. This is expected from higher surface migration velocities of adatoms and lower oxygen incorporation at higher growth temperature.

On the contrary, a decrease in the PL integrated intensities for (111) AlGaAs as the growth temperature is increased cannot be explained by the above argument.

Furthermore, to characterize InGaAs growth on (111)B GaAs, Chin et al. [17] have grown a 20 Å $In_{0.21}Ga_{0.79}As$ QW at 550° C, for which the linewidth of the PL spectrum at 2.2 K is extremely small (only 3.0 meV), showing the high quality of the growth.

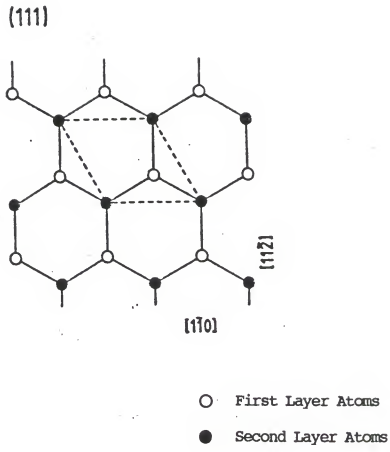

Fig 2.3 A (111) surface of a diamond type crystal [24].

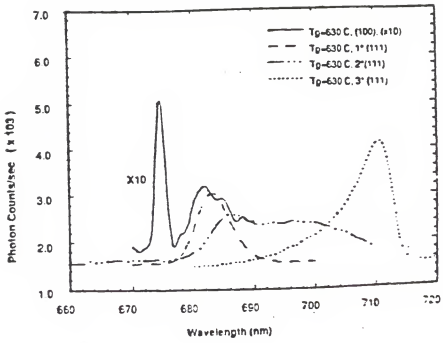

Fig 2.4 13 K PL of 2.0 μm-thick $Al_{0.22}Ga_{0.78}As$ grown at 630°C [18].

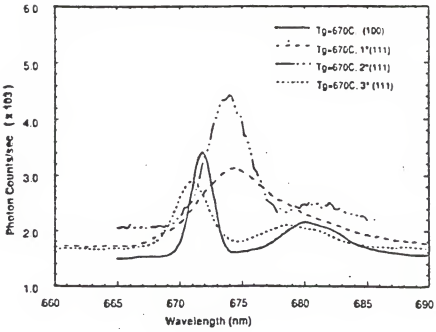

Fig. 2.5 13 K PL of 2.0 μm-thick $Al_{0.22}Ga_{0.78}As$ grown at 670°C [18].

The InGaAs/AlGaAs structures we investigated were grown on 2° misoriented undoped (111)B and (100) GaAs substrates. The AlGaAs and the InGaAs layers were grown at substrate temperatures of 670 and 550 °C respectively. The reason for choosing 2° misoriented (111)B GaAs substrate and a growth temperature of 670°C can be clearly seen in Figs 2.4 and 2.5. The PL peak intensity of the AlGaAs layer grown at 670°C and on 2° misorientation (111)B GaAs is much higher than all other misorientations at both growth temperatures, and its FWHM is also smaller than that of the 3° misoriented substrate.

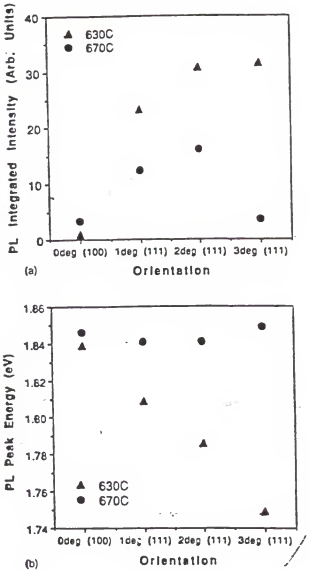

Fig. 2.6 Substrate orientation dependence of [18]
(a) PL integrated intensity.
(b) PL peak energy
for $Al_{0.22}Ga_{0.78}As$ grown at 630 and 670°C.

CHAPTER 3
CHARACTERISTICS OF STRAINED MQW STRUCTURES GROWN ON (111)B GaAs SUBSTRATES

3.1 Introduction

Strained MQW structures grown on (111)B GaAs substrates differ significantly from their (100) counterparts. Layers grown along the (111) direction exhibit an increase in the value of the heavy hole effective mass conversely rendering a lower value for the HH1 transition in the wells and decreasing the C1-HH1 transition energy.

Moreover, the presence of strain due to the growth of lattice mismatched layers(namely InGaAs on (111)B GaAs) produce a strain-induced electric field in these layers due the piezoelectric nature of the (111) grown layers, yielding a shift toward a lower C1-HH1 transition energy due the Quantum Confined Stark Effect (QCSE).

On the other hand, due to the hydrostatic and shear strain present in the lattice mismatched layers, the conduction to the valence band transition energy will go up significantly in the case of (111) grown layers compared to that of (100) grown layers.

After discussing the above mentioned characteristics, we introduce our suggested p-i-n structures grown on (111)B and

(100) GaAs. Then, the characteristics of the layers grown along these orientations will be discussed showing the effect that this growth orientation has on the performance of these layers. Finally, we explain the reasons behind choosing these structures, showing the advantage that our structures has over other structures introduced by previous researchers, and their possible use as optical devices, mainly Self-Electrooptic Effect Devices (SEEDs).

3.2 Characteristics of Strained Structures on (111)B Substrates

3.2.1 Effective Mass Changes due to the Growth Orientation

The effective mass change affects the quantization shift in the grown layers and is also understood to influence the optical matrix element and the density of states. It was shown [25-27 that the heavy hole effective mass along the growth axis changes considerably between the (100) and (111) growth orientations. The heavy hole and light hole effective masses along the growth axis for the (100) and (111) oriented structures are expressed as [14]

$$m_{\substack{lh \\ hh}}^{(100)} = \frac{m_o}{\gamma_1 \pm 2\gamma_2} \tag{3.1}$$

$$m_{\substack{lh \\ hh}}^{(111)} = \frac{m_o}{\gamma_1 \pm 2\gamma_3} \tag{3.2}$$

where γ_1, γ_2 and γ_3 are the Luttinger-Kohn [28,29] parameters and m_o is the free electron mass.

Using the values given in Table 3.1, $m_{hh}(111)$ for GaAs, for example, is $0.917m_o$ while $m_{hh}(100)$ for the same material is $0.353m_o$, where m_o is the free electron mass. Since the (111) oriented heavy hole mass is 2.6 times higher than that of the (100) orientation, the quantized energies in the QWs for heavy hole subbands in the (111) structure therefore are smaller. As a result, even higher order transitions between electron and heavy hole subbands are expected to be observed in transmission measurements for the (111) oriented QWs. On the other hand, the electron effective mass is the same for both (111) and (100) grown samples, while the light hole effective masses vary only by a small amount ($m_{lh}(111)=0.07m_o$ and $m_{hh}(100)=0.08m_o$ for GaAs). Thus, the light hole related transitions energies are considered to be almost the same in (100) and (111) oriented QWs.

Table 3.1
Luttinger-Kohn Parameters

	γ_1	γ_2	γ_3
GaAs	7.65	2.41	3.28
InAs	19.67	8.37	9.29
AlAs	4.04	0.78	1.57

3.2.2 Piezoelectric Effect

Unlike (100) oriented strained layers, (111) strained layers of piezoelectric active materials, such that zinc-blende compounds, have built-in longitudinal electric fields [6]. Piezoelectric active crystals are a class of crystals which produce a macroscopic electric polarization when stressed. Because electric polarization is a vector, crystals which have a center of inversion symmetry cannot be polarized by stress and therefore cannot be piezoelectric [30]. Zinc-blende crystals lack inversion symmetry and are known to be piezoelectrically active [31]. Stressing a crystal produces a microscopic displacement, or strain, of the atoms from their equilibrium positions. If the strain results in an unequal motion of the positive charges with respect to the negative charges, then an electric polarization will be produced. Misfit strain, generated in a crystal during pseudomorphic epitaxy, is accommodated by the competing process of elastic deformation and misfit dislocation formation, both of which act to minimize the strain energy of the system [32]. In sufficiently thin overlayers, where misfit dislocations are energetically not favored, the overlayer is constrained to grow in registry with the negligibly strained substrate. In this way, the layer is subjected to a biaxial stress, in the plane of the growth, which induces an elastic deformation, leaving the overlayer tetragonally distorted [33]. Although both (100)

and (111) oriented strained crystals are grown under biaxial stress and experience a longitudinal tetragonal distortion, only the (111) growth axis strained layers produce a macroscopic polarization. This polarization is given by

$$P_i = e_{14}\, e_{jk} \tag{3.3}$$

where P_i is the induced polarization, e_{14} is the piezoelectric constant [34], and e_{jk} is the symmetrized strain component [35]. However, diagonal components of the strain matrix (e.g. e_{xx}) do not induce a polarization (i.e., $e_{11} = 0$) in the zinc-blende materials [31]. The sign of the polarization vector in a material depends on whether it has the larger or smaller lattice constant and on the sign of the piezoelectric coefficient. The common III-V semiconductors have a negative piezoelectric coefficient [35]. A III-V semiconductor with the larger lattice constant in a strained layer superlattice will have the polarization vector pointing from the A (cation) to the B (anion) face. A III-V semiconductor with the smaller lattice constant will have the polarization vector pointing from the B to the A face. Thus, for a strained-layer superlattice with [111]-growth axis of two III-V semiconductors, polarization vectors along the growth axis, and of opposite sign in the two materials(InGaAs and AlGaAs for the case studied here), are induced by the piezoelectric effect. Furthermore, for the case we are about to present where the InGaAs layer is under biaxial

compression, the strain-induced electric field will point toward the substrate for a (111)B (i.e. As terminated) substrate (see Fig. 3.1).

Because the three off-diagonal stress components are equal, the components of the polarization vector are equal and the polarization vector is in the [111]-growth direction. Thus, there are four unknowns: a diagonal and an off-diagonal strain component in each material. Requiring that the strain-distorted lattice-translation vectors of the two materials have equal projections on the plane normal to the growth direction gives

$$(1 + \varepsilon^a_{xx}) - \frac{\varepsilon^a_{xy}}{2} a^a = (1 + \varepsilon^b_{xx}) - \frac{\varepsilon^b_{xy}}{2} a^b \tag{3.4}$$

where a^i is the lattice constant of material i. The mechanical energy density of the superlattice is minimized with respect to the strain components subject to the condition of Eq. (3.4). This procedure gives

$$\varepsilon^a_{xx} = \frac{\left(\frac{a^b}{a^a}\right) - 1}{\left[(1+A^a) + (1+A^b)\, B \left(\frac{h_a}{h_b}\right)\right]} \tag{3.5a}$$

$$\varepsilon^b_{xx} = -\frac{h_a}{h_b} B\, \varepsilon^a_{xx} \tag{3.5b}$$

$$\varepsilon^a_{xy} = -2\, A^a\, \varepsilon^a_{xx} \tag{3.5c}$$

$$\varepsilon^b_{xy} = -2\, A^b\, \varepsilon^b_{xx} \tag{3.5d}$$

$$A^i = \frac{C^i_{11} + 2\,C^i_{12}}{4\,C^i_{44}} \tag{3.5e}$$

$$B = \frac{C^a_{11} + 2\,C^a_{12}}{C^b_{11} + 2\,C^b_{12}} \tag{3.5f}$$

where h_i is the layer thickness of material i and the C's are the elastic coefficients of the materials a and b. For (111) grown layers, the diagonal stress components (ε^i_{xx}, ε^i_{yy}, ε^i_{zz}) do not induce any internal electric field, only off-diagonal stress components (ε^i_{xy}, ε^i_{yz}, ε^i_{zx}) need to be considered. The strain induced electric polarization P_i will lead to electric field E_i given by

$$D_i = \varepsilon_o\, E_i + \chi\, E_i + P_i \tag{3.6}$$

where χ is the susceptibility and D_i is the electric displacement. If there are no external charges, D_i vanishes, and the electric field reduces to

$$E_i = -\frac{e_{14}\varepsilon_{jk}}{\varepsilon_o \varepsilon} \tag{3.7}$$

where $\varepsilon = 1 + \chi$ is the low frequency dielectric constant.

The strain induced-field tends to shift the electron and hole quantized energies by QCSE, thus reducing the effective band gap [14].

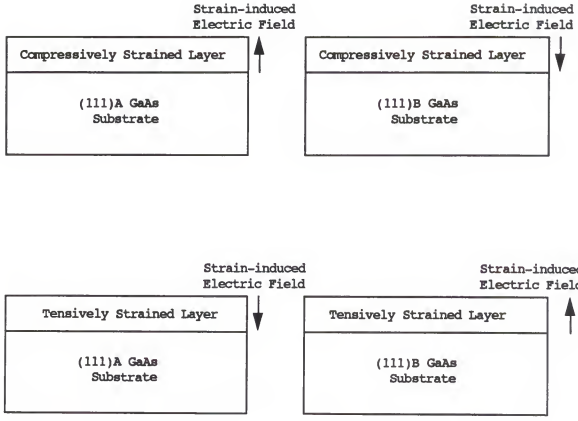

Fig. 3.1 Strain-induced Electric Field .

3.2.3 Band Structure Modification due to Strain Effect

For conditions that the thickness of the layer is less than the critical thickness [36-38], the strain is confined in the layer without the formation of dislocations (pseudomorphic growth). In this case, the lattice constant of the epitaxial layers in the plane perpendicular to the growth axis is equal to that of the substrate. As a first-order perturbation of the strain Hamiltonian, the strain induced band structure modification in the (111) grown layers can be written as

$$\Delta E_c = 3\, a_c\, \varepsilon_{xx} \tag{3.8}$$

for the conduction band and

$$\Delta E_{\substack{hh \\ lh}} = 3\, a_v\, \varepsilon_{xx} \pm \sqrt{3}\, d\, \varepsilon_{xy} \tag{3.9}$$

for the heavy hole band (+) and the light hole band (-), respectively [14], a_c and a_v are the conduction and the valence bands hydrostatic deformation potentials, and d is the shear deformation potential. In Eqs. 3.8 and 3.9, energy positive directions are set to be opposite between conduction and valence band. It was shown [33] that, for compressively strained layers (0.5 % strain) grown on (100) and (111) oriented InP substrates, the valence band splitting due to shear strain was very similar, whereas the bandgap change

due to hydrostatic strain was much larger for (111) than for (100). The C1-HH1 transition for the (111) grown layers was 33 meV higher than the unstrained case while for (100) it was only 17 meV higher (see Fig. 3.2).

3.3 A Study of (111)B Grown Strained MQW Structures

3.3.1 Introduction

The structures investigated are p-i-n diodes, with the wells imbedded in the intrinsic region of the diode, having different In compositions and therefore different strain and built-in strain-induced electric fields.

The p-i-n structures were grown simultaneously by MBE on (111)B and (100) GaAs substrates. A schematic of the structures is shown in Fig.3.3 (a) and (b). The first structure (**S1**) is composed of a 0.8 μm n^+ GaAs layer, followed by a 2.5 μm n^+ $Al_{0.2}$ $Ga_{0.8}As$ layer, and undoped 250 nm $Al_{0.11}$ $Ga_{0.89}As$ layer, then the MQW region (10 periods, 15 nm $Al_{0.2}$ $Ga_{0.8}As$ / 10 nm $In_{0.1}Ga_{0.9}As$), then an undoped 250 nm $Al_{0.11}$ $Ga_{0.89}As$ layer, and a 1 μm p^+ $Al_{0.2}Ga_{0.8}As$ layer capped with a 50 nm p^+ GaAs. The structures were designed to work as single mode slab waveguides for wavelengths 0.8-1.3 μm. The second structure (**S2**) is similar to the first but has $Al_{0.17}Ga_{0.83}As$ instead of $Al_{0.11}$ $Ga_{0.89}As$ cladding layer and also $In_{0.05}Ga_{0.95}As$ instead of $In_{0.1}Ga_{0.9}As$ in the well.

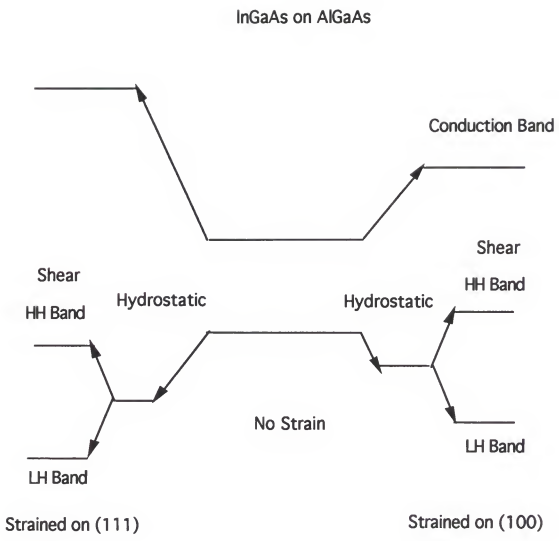

Fig 3.2 Different energy band shifts for (100) and (111).

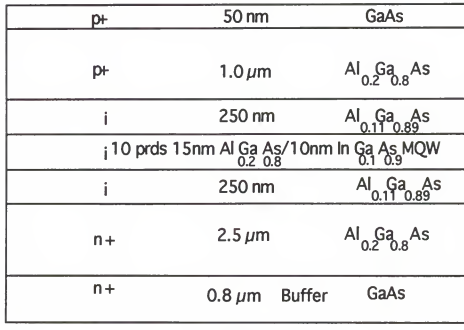
p+ 50 nm GaAs
p+ 1.0 μm $Al_{0.2}Ga_{0.8}As$
i 250 nm $Al_{0.11}Ga_{0.89}As$
i 10 prds 15nm $Al_{0.2}Ga_{0.8}As$/10nm $In_{0.1}Ga_{0.9}As$ MQW
i 250 nm $Al_{0.11}Ga_{0.89}As$
n+ 2.5 μm $Al_{0.2}Ga_{0.8}As$
n+ 0.8 μm Buffer GaAs
GaAs susbtrate

S1

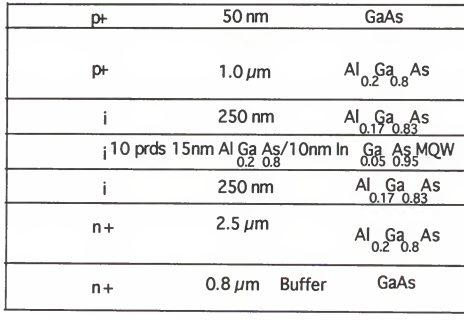
p+ 50 nm GaAs
p+ 1.0 μm $Al_{0.2}Ga_{0.8}As$
i 250 nm $Al_{0.17}Ga_{0.83}As$
i 10 prds 15nm $Al_{0.2}Ga_{0.8}As$/10nm $In_{0.05}Ga_{0.95}As$ MQW
i 250 nm $Al_{0.17}Ga_{0.83}As$
n+ 2.5 μm $Al_{0.2}Ga_{0.8}As$
n+ 0.8 μm Buffer GaAs
GaAs susbtrate

S2

Fig. 3.3 Structure of proposed p-i-n devices.

3.3.2 Kronig-Penney Model

A theoretical model based on the Kronig-Penney method [39] was used to calculate the C1-HH1 MQW transitions in the above mentioned structures.

The heavy hole effective masses of the GaAs, AlAs and InAs are calculated using equation 3.2. Then, the mhh of InGaAs and AlGaAs are obtained using the following interpolation

$$m_{hhAlGaAs} = x\, m_{hhAlAs} + (1-x)\, m_{hhGaAs} \tag{3.10}$$

$$m_{hhInGaAs} = y\, m_{hhInAs} + (1-y)\, m_{hhGaAs} \tag{3.11}$$

Similarly, the electron effective masses is of AlGaAs and InGaAs are given by

$$m_{cAlGaAs} = m_o*(0.0665 + 0.083\, x) \tag{3.12}$$

$$m_{cInGaAs} = m_o*(y\ 0.023 + (1-y)\ 0.067 \tag{3.13}$$

where x and y are the Al and In fractions, respectively and m_o is the free electron mass.

In the same manner, the lattice constants for AlGaAs and InGaAs are obtained by interpolating the values of the lattice constants of GaAs, AlAs and InAs mentioned in Table 3.2.

The bandgap energies of the AlGaAs barriers and the InGaAs wells are determined using the following equations :

$$Eg_{AlGaAs} = 1.424 + 1.266\ x + 0.26\ x^2 \tag{3.14}$$

$$Eg_{InGaAs} = 0.36 + 0.505\ (1-y) + 0.555(1-y)^2 \tag{3.15}$$

$$Eg = Eg_{AlGaAs} - Eg_{InGaAs} \tag{3.16}$$

The relation between the conduction band discontinuity ΔE_C and Eg is for $InGaAs/Al_{0.2}Ga_{0.8}As$ quantum well structures given by [40]

$$\Delta E_C = 0.6\ Eg \tag{3.17}$$

while the valence band discontinuity is given by

$$\Delta E_V = Eg - \Delta E_C \tag{3.18}$$

The quantization energy, E_{c1}, of the first electron level in the conduction band is equal to the energy for which

$$\frac{\gamma^2 - \alpha^2}{2\alpha\gamma} \sinh \gamma L_b \sin \alpha L_z + \cosh \gamma L_b \cos \alpha L_z = -1 \tag{3.19}$$

$$\alpha = \sqrt{\frac{8\pi^2 E_{c1} m_{c_{InGaAs}}}{h^2}} \tag{3.20}$$

$$\gamma = \sqrt{\frac{8\,\pi^2\,(\Delta E_c - E_{c1})\,mc_{InGaAs}}{h^2}} \qquad (3.21)$$

where L_b and L_z are the barrier and well width, respectively.

Similarly, the value of Ev1, the first electron level in the valence band is acquired using the equations above, after exchanging mc_{InGaAs} by mhh_{InGaAs}, Ec1 by Ev1 and ΔE_C by ΔE_V. Fig. 3.4 shows the C1-HH1 transition without the presence of strain or electric field.

Table 3.2
Parameters of GaAs, AlAs, InAs and InGaAs

	a_o (Å)	$C_{11}*10^{11}$ dynes/cm^2	$C_{12}*10^{11}$ dynes/cm^2	$C_{44}*10^{11}$ dynes/cm^2	e_{14}
GaAs	5.6532	11.810	5.32	5.940	-0.1600
AlAs	5.6611	12.020	5.70	5.870	-0.2250
InAs	6.0584	8.330	4.53	3.960	-0.0450
InGaAs (5% In)	5.6734	11.636	5.28	5.841	-0.15425
InGaAs (10% In)	5.69372	11.462	5.241	5.742	-0.1485

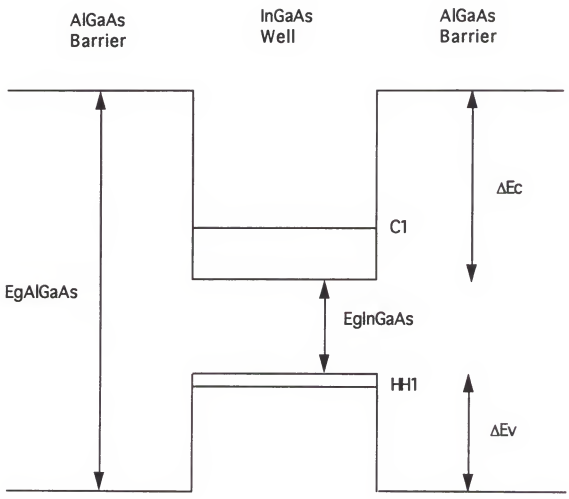

Fig. 3.4 Energy band structure of a QW with no electric field present.

3.3.3 Strain Effect on C1-HH1 Transition Energy

would move the electron to heavy hole transition to a higher energy. For the (111)B grown layers, this shift can be determined by replacing the values of a_c, a_v and d for each InGaAs composition in equations 3.8-9. For the same structures grown on (100) GaAs substrates, the hydrostatic and shear strains will cause a similar shift but by a different amount. The change in this case is given by [41]

$$\Delta E_{hh} = \left[-2\, a\left(\frac{C_{11} - C_{12}}{C_{11}}\right) + b\left(\frac{C_{11} + 2\,C_{12}}{C_{11}}\right)\right] \varepsilon \qquad (3.22)$$

Where ΔE_{hh} is the shift of the heavy hole valence band, ε is the biaxial strain parallel to [100] and [010] directions, taken here to be the mismatch Δa given by

$$\Delta a = (a_{InGaAs} - a_{AlGaAs})/a_{AlGaAs} \qquad (3.23)$$

a and b are the hydrostatic and the shear deformation potentials, respectively. The values of a and b are given in Table 3.3 for GaAs and InAs. These values for InGaAs are calculated by interpolating their respective binary values.

Comparing the amount of shift between the (100) and the (111)B grown structures will show a higher value in the case of the latter. This presents an advantage in using the

(111)B grown structures yielding higher change in the transition energies for the same Δa.

Table 3.3
a, b, ac, av and d Parameters of GaAs and InAs

	GaAs	InAs
a(eV)	2.7	2.5
b(eV)	-1.7	-1.8
a_c(eV)	-18.3	-11.7
a_v(eV)	-4.8	-5.2
d(eV)	-4.4	-4.6

3.3.4 Electric Field Effect on QWs

The presence of strain-induced electric field in the wells will cause a red shift in the transition energies. This can be explained by the Quantum-Confined Stark Effect (QCSE). This effect can be explained as follows. An electric field perpendicular to the quantum well layers pulls the electrons and holes towards opposite sides of the layers resulting in an overall net reduction in energy of an electron-hole pair and a corresponding Stark Shift in the exciton absorption (see Fig. 3.5). The walls of the quantum well impede the electron and hole from tunneling out of the well in rapid field ionization. Because the well is narrow

(in our case 100Å) compared to the three dimensional (3D) exciton size (e.g. 300Å), the electron-hole interaction, although weakened by the separation of electron and hole, is still strong and well defined excitonic states can still exist. Kajikawa et al.[42] have showed an increase in the rate of energy shift of the C1-HH1 exciton under the application of an electric field for (111) QWs over that for (100) QWs having the same width.

To determine to what extent the presence of the strain-induced electric field would affect the C1-HH1 transition, we will use the effective infinite well model reported by Miller et al. [11]. This model uses the infinite well model with effective well widths assigned separately for the electron and the heavy hole, instead of the actual well size, in order to obtain the correct zero-field energies. The exact solution for a particle in an infinite well in the presence of a uniform static field is explained as follows. It was found [43-45] that if the particle is restrained to stay within an infinitely deep well, an exact solution can be obtained for any value of the static field. This is the consequence of the boundary conditions imposed upon the wave function $\zeta(z)$, i.e., $\zeta(\pm\frac{1}{2} L_z) = 0$ for any field.

The Schrodinger equation can be written

$$\frac{h^2}{8\pi^2 m^*} \frac{d^2}{dz^2} \zeta(z) - (W + e F_{\perp} z)\zeta(z) = 0 \qquad (3.24)$$

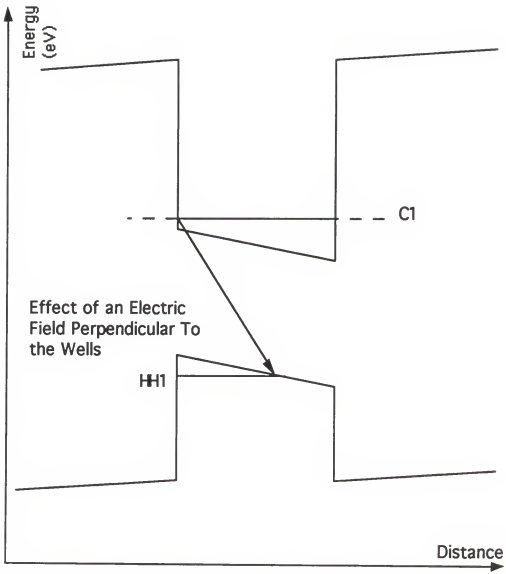

Fig. 3.5 Effect of electric field on C1-HH1 energy transition.

where h is the Boltzmann constant, W is the energy, and $F_\perp$ is the perpendicularly applied electric field.

The zero-field solutions are known, i.e.,

$$W_n = \frac{h^2}{8\pi^2 m^*}\left[n\,\frac{\pi z}{L_z}\right]^2 \tag{3.25}$$

$$\zeta_n(z) = \left[\frac{2}{L_z}\right]^{\frac{1}{2}} \cos\left[n\,\frac{\pi z}{L_z}\right] \tag{3.26}$$

It is therefore natural to use the energy of the ground state as the unit of energy

$$W_1 = \frac{h^2}{8\pi^2 m^*}\left[\frac{\pi z}{L_z}\right]^2 \tag{3.27}$$

and as unit of field F_1 such that $eF_1 = W_1$.

In order to transform Equation 3.24 into the Airy differential equation it is convenient to use a new variable z.

$$z = -\left[\frac{8\,\pi^2\,m^*}{(ehF_\perp)^2}\right]^{\frac{1}{3}} (W + e\,F_\perp\,z) \tag{3.28}$$

Note that $W + e\,F_\perp\,z$ represents the kinetic energy and that $\left[8\,\pi^2\,m^*/(ehF_\perp)^2\right]^{\frac{1}{3}}$ has the dimensions of energy. z is therefore

a normalized kinetic energy. The new form of Equation 3.24 can be written

$$\frac{d^2}{dZ^2}\,\zeta(Z) - Z\,\zeta(Z) = 0 \tag{3.29}$$

Whose solutions are of the form

$$\zeta(Z) = a\,Ai(Z) + b\,Bi(Z) \tag{3.30}$$

Where a and b are two constants and Ai(Z) and Bi(Z) are the Airy functions [46]. The boundary conditions are

$$\zeta(Z_+) = \zeta(Z_-) = 0 \tag{3.31}$$

where $Z_\pm = Z(\pm \frac{1}{2} L_z)$. If we measure the energies and fields in units W_1 and F_1, i.e.,

$$w = \frac{W}{W_1} \tag{3.32a}$$

$$f = \frac{F_\perp}{F_1} \tag{3.32b}$$

Then

$$Z_\pm = \left[-\frac{\pi}{f}\right]^{\frac{2}{3}} (w \pm \tfrac{1}{2} f) \tag{3.33}$$

and

$$Ai(Z_+)\,Bi(Z_-) - Ai(Z_-)\,Bi(Z_+) = 0 \qquad (3.34)$$

which completely determines the eigen energy. Note that in the normalized form the effective mass and the well thickness have disappeared. Therefore Equations 3.33 and 3.34 are universal. Figure 3.6 shows the universal curve for the energy for the first state in an infinite quantum well in the presence of a uniform electric field perpendicular to the walls.

The InGaAs wells suffer a compressive strain when grown on GaAs substrates (AlGaAs has practically the same lattice constant as GaAs) due to the fact that InGaAs has a higher value of the lattice constant. The presence of compressive strain and the fact that the layers are grown on (111)B GaAs substrates (as was previously mentioned), would direct the electric field vector towards the substrate (see Fig. 3.7).

Figure 3.8 shows the energy band structure for the (100) and the (111)B grown layers. For the structures that we are suggesting, the value of this field in sample **S1** is calculated to be 1.1 10^5 V/cm, while for sample **S2** it is 5.5 10^4 V/cm. Using the effective infinite well method described previously, the decrease of the C1-HH1 transition energy to a lower value is found to be 24 meV and 11 meV for **S1** and **S2**, respectively.

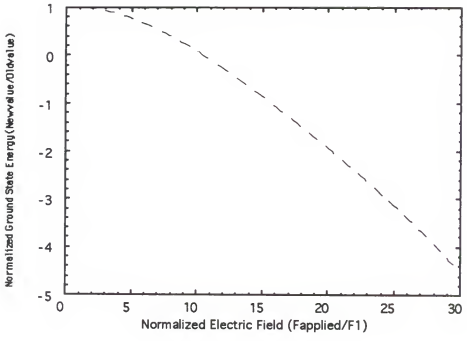

Fig. 3.6 Universal curve for the energy of the first state in an infinite quantum well in the presence of a uniform electric field perpendicular to the walls of the well.

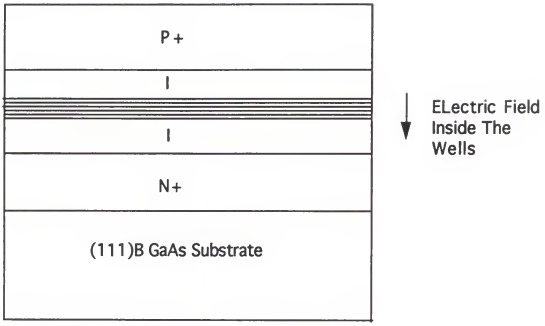

Fig. 3.7 Electric field direction inside the wells.

3.3.5 Combined Effects

Finally, after presenting the effects of the effective mass, the strain, and the presence of strain-induced electric field on the C1-HH1 transition energy, we add these effects together for the (100) and the (111)B grown structures. Figure 3.9 shows clearly that for the same structures grown on (100) and (111)B GaAs the C1-HH1 is much higher in the latter due to higher strain induced energy shift.

The computer programs written to calculate the C1-HH1 transition energy for (100) and (111) grown MQWs are presented in Appendices A and B.

3.3.6 Advantages of the Proposed Structures

Most of the reported research to this date used InGaAs/GaAs SQWs [9,14,47] with thick barriers, eliminating strain in the GaAs barrier layers. We propose having an InGaAs/AlGaAs structure instead of the InGaAs/GaAs structure because in the latter the barriers are not high enough to stop the tunneling of electrons in the QWs under bias and because the light hole energy band is not confined within the quantum well because of the small valence band offset [48].

Furthermore, the use of AlGaAs as barriers instead of GaAs assures the elimination of any blurring of the QW's absorption by the absorption of the barrier's material [49].

Under bias, the C1-HH1 transition energy moves towards

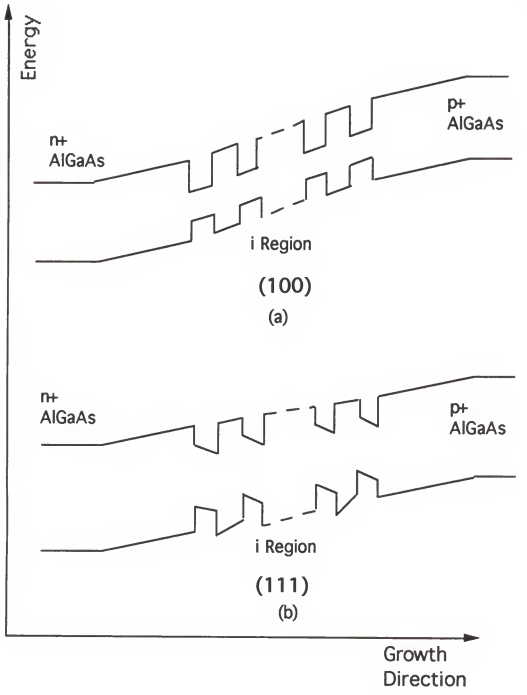

Fig. 3.8 (a) Energy band structure of (100) grown samples.
(b) Energy band structure of (111) grown samples.

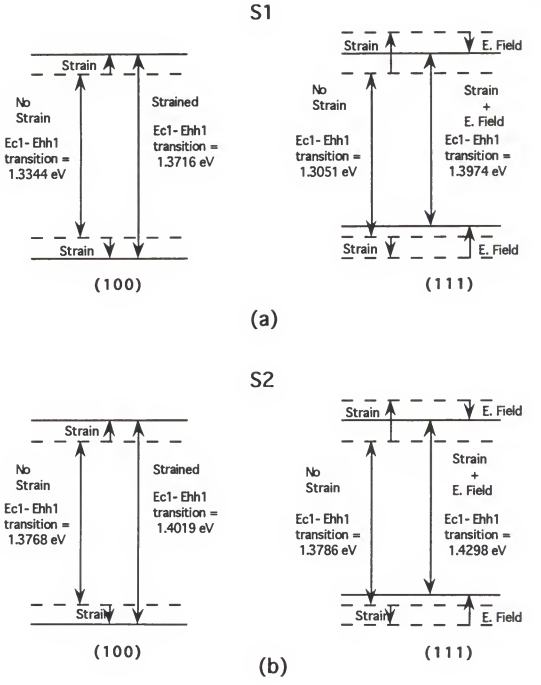

Fig. 3.9 Combined effects determining C1-HH1 transition energy.
(a) For structure S1 (In 10%).
(b) For Structure S2 (In 5%).

higher energy, while the barriers' bandgap transition goes to a lower energy. As shown in Figure 3.10 the GaAs transition energy can cross that of the QW's under appropriate bias, while for AlGaAs this situation is not likely to occur until an extremely high bias.

In the next chapters we will investigate these properties, especially the presence of the strain-induced electric field.

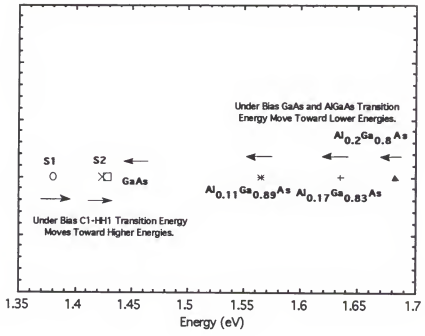

Fig 3.10 The effect of electric field on the transition energy in the wells' in S1-S2, and in the AlGaAs and GaAs layers.

CHAPTER 4
EFFECT OF OPTICAL EXCITATION AND MECHANICAL STRESS ON THE CHARACTERISTICS OF THE STRUCTURES

4.1 Introduction

One of the methods suggested to prove the existence of a strain-induced electric field in the wells is to use PL measurement of the QW peak position and its shift under increase of laser intensity. It was reported [49] that the photocreation of electron-hole pairs would cause the screening of such electric field. Moise et al.[49] showed a substantial shift of the strained QW peak, grown on (111)B GaAs, to a higher energy under increased optical excitation.

Tailoring the band gap transition energies can be achieved by subjecting a sample to mechanical strain which would play the same role as the one played by the growing mismatched layers. But the advantage here is that an energy shift can be controlled by placing the sample on a transducer and adjusting the applied voltage to the desired value. This controlled transition energy shift would selectively change the band gap of the sample thus changing its optical characteristics. The increase in band gap due to compressive strain has a reverse effect on the refractive index. While

under tensile strain the band gap decreases in urn increasing the refractive index. We will investigate the effect that applied mechanical tension on (111) grown samples has on the absorption peak position and on its intensity.

4.2 Effect of Optical Excitation

Shining a laser beam with a photon energy higher than the expected transition energy for the QWs, will cause the creation of an electron-hole pair, with the electron acquiring enough energy to be transferred to the conduction band. Once there, the electron is bound to come back to a lower energy state passing by the quantized energy states (back to the valence band) releasing in the process a photon whose energy corresponds to the energies of these states (see Fig. 4.1).

The photons created in the process are passed through a monochrometer that selects the appropriate light wavelength, via a grating. These photons having a certain wavelength are then detected by a thermoelectrically cooled photomultiplier tube. The latter is connected to a computer where the information about the intensity and the wavelength of the radiation is stored.

As the intensity of the applied laser light is increased, the number of created electron-hole pairs increases given rise to an electric field that would

partially screen the strain-induced electric field present in the QWs. As was mentioned in the previous chapter, the presence of an electric field inside a QW will cause the C1-HH1 transition energy to be reduced. So an increase in the intensity of the optical excitation would yield a shift of the PL peak position of the QW to a higher energy only in samples where a built-in electric field (111 grown samples) already exists.

Moise et al. [49] reported that a strain induced electric field in the QWs of 9×10^4 V/cm corresponds to an interface charge density of 6.6×10^{11} cm^{-2}. Therefore, for the structures at hand, the density of carriers needed for complete screening of the internal fields comes out to be 8.067×10^{11} cm^{-2} for the sample S1 (10% In), and 4.034×10^{11} cm^{-2} for sample S2 (5% In).

4.3 PL Measurements

The Photoluminescence setup used in the measurements is depicted in Fig. 4.2. The PL was measured at 13 K using a 0.64 m spectrometer. A 40 mW Ar^+-ion laser operating at 514.5 nm was used as the excitation source and the signal was detected with a thermoelectrically cooled photomultiplier. All the measurements were done under identical conditions for all samples under study in order to compare the results.

From the results presentedin Figs.4.3-6, it can be seen that in the case of the (111) grown layers the intensity of

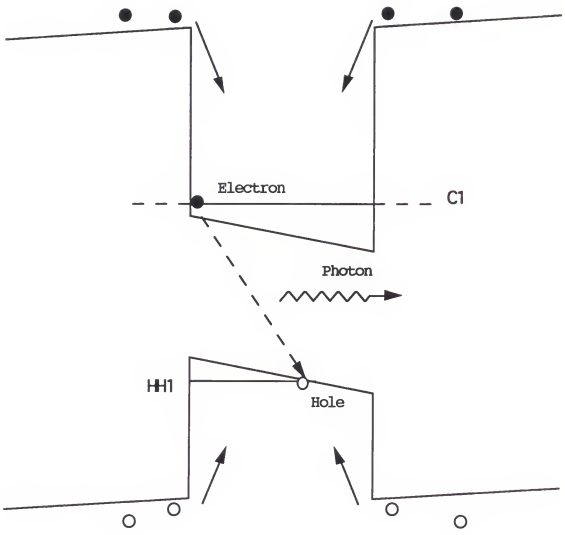

Fig. 4.1 The e^- transition from C1 to HH1.

the MQW luminescence is 1.2 to 2 times stronger than that of the (100) grown layers, and the FWHM for (111) is smaller than that of the (100) grown MQWs, implying an increase in the optical matrix element [7,14]. This shows that the optical quality of (111) grown material is excellent and is better than the layers grown on (100) [18].

When increasing the excitation power the number of carriers inside the wells increases causing the screening of the strain-induced electric field. This will cause the energy bands to move closer to a flat band case producing higher luminescence intensity and lower FWHM. The PL measurements depicted in Figs 4.3,5 show a shift of the MQW peak for the (111) samples toward higher energies and a decrease in the FWHM with increasing laser intensity while the same trend is absent for (100) (Figs. 4.4,6). This confirms the presence of a built-in electric field inside the (111) grown layers.

Using the Kronig-Penney model presented in Chapter 3, we generated Figs. 4.7 and 4.8 that show the change in the MQW peak energy when the strain-induced electric field is screened for the structures S1 and S2, respectively. For the levels of power used in the measurements, the shifts of MQW are measured to be 2.44 meV and 0.5 meV for S1 and S2, respectively.

4.4 Amount of E-Field Screening

In order to determine the intensity of the light reaching the wells, we need to know the laser intensity at the surface of the sample, the power reflection from both sides of the glass window of the cryostat and from the top of the sample itself, and the absorption of the layers atop of the wells' region.

The equation for the reflectivity at normal incidence is given by [50],

$$R = \frac{(n_1 - n_2)^2}{(n_1 + n_2)^2} \tag{4.1}$$

where n_1 and n_2 are the refractive indices of the adjacent regions (air-glass, glass-air, and air-sample).

For the cryostat glass window, the refractive index is 1.5 yielding a reflectivity of 0.04 for each of the sides of the glass. The refractive index of GaAs is 4.14 (see Chapter 5 for refractive index calculations) at 514.5 nm producing a reflectivity of 0.373. The combination of all these factors will reduce the intensity by a factor of 0.5778 upon reaching the sample's surface.

To be able to change the intensity of the laser excitation neutral density filters were placed in the path of the laser light. Full power in the case of S1 is 24.58 mW, with the neutral density filter ND1 it is 2.458 mW and with

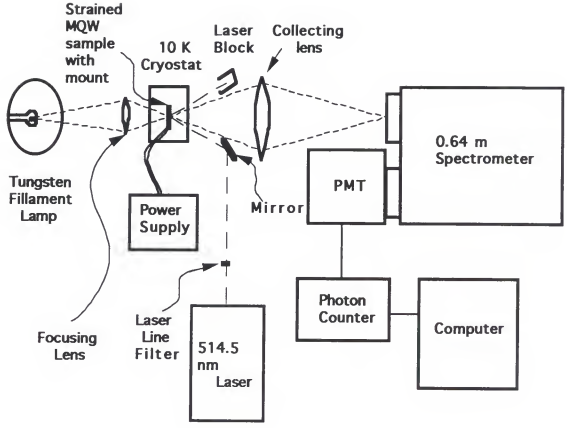

Fig 4.2 PL setup.

ND2 it is 0.5 mW. For S2, Full power is 13.76 mW, ND1 is 1.87 mW, and ND2 is 0.5 mW.

The beam coming out of the laser is considered to be a Gaussian beam with a $TEM_{0,0}$ mode [51]. The equations governing the spot size for such a beam are :

$$w^2(z) = w_o^2 \left[1 + \left(\frac{z}{z_o}\right)^2\right] \tag{4.2}$$

$$z_0 = \frac{n\pi w_o^2}{\lambda} \tag{4.3}$$

where w_o is the spot radius at a position z=0, w(z) the spot size at a position z, and n is the medium's refractive index, and w_s at the sample's surface was determined to be 36 μm. Using the above information, the laser's intensity can be derived from :

$$I_s = \frac{P_s}{\pi w_s^2} \tag{4.4}$$

where I_s, P_s and w_s are the laser intensity, power and spot size at the surface of the sample, respectively.

After combining these different factors, we can calculate the intensity of the light hitting the sample's surface. For full laser power in the case of S1 the intensity is 571.51 W cm^{-2}, with ND1 in place it is 57.15 W cm^{-2}, and with ND2 in place it is 11.62 W cm^{-2}. In the case

of S2 Full corresponds to an intensity of 320 W cm^{-2}, with ND1 43.48 W cm^{-2}, and with ND2 11.62 W cm^{-2}.

The absorption loss caused by the presence of layers atop of the QW region is given by [52]

$$I = I_o \, e^{-\alpha L} \tag{4.5}$$

$$\alpha = A \, (h\nu - Eg)^{\frac{1}{2}} \tag{4.6}$$

where I is the final intensity, I_o is the initial intensity, α is the absorption coefficient, A is a constant, $h\nu$ is the energy of the laser light, Eg is the bandgap energy, and L is the width of the layer.

We assume that all the e-h pairs created in the p+ layers will be collected in the i region. Considering that the spot size does not change significantly when traveling through these layers, the intensity reaching the wells suffers some absorption in the AlGaAs layer atop the QW region (reduction of 40%). For sample S1 the intensity reaching the wells is about 157 W cm^{-2} and for sample S2 it is about 163 W cm^{-2} for Full power.

Moise et al. [49] showed that at a wavelength of 514.5 nm the intensity needed to create $2x10^{12}$ cm^{-2} e-h pairs is 413.6 W cm^{-2}. In our case, 200 (571.51 x 0.5778 x 0.6) W cm^{-2} would yield $9.65x10^{11}$ cm^{-2} e-h pairs, and 112 (320 x 0.5778 x 0.6) W cm^{-2} would yield 5.41 $10^{11}xcm^{-2}$ e-h pairs, causing a total screening of the electric field.

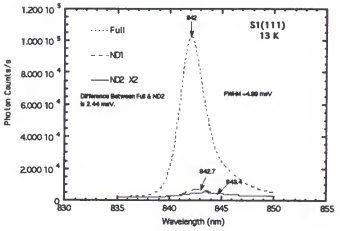

Fig 4.3 QW peak shift with increased laser power.

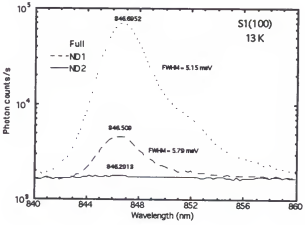

Fig 4.4 QW peak shift with increased laser power.

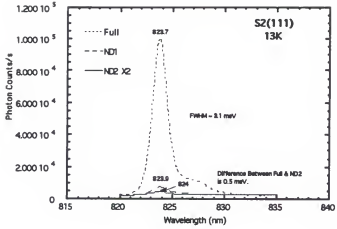

Fig 4.5 QW peak shift with increased laser power.

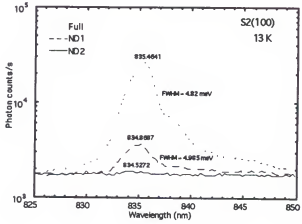

Fig 4.6 QW peak shift with increased laser power.

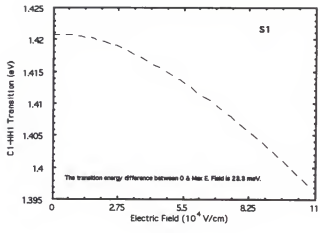

Fig. 4.7 Effect of screening the E field in the QWs.

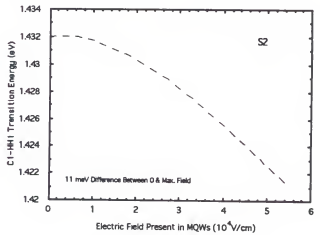

Fig. 4.8 Effect of screening the E field in the QWs.

4.5 Mechanical Strain Effect

In order to investigate the effect that applied mechanical strain has on the optical characteristics of (111) grown samples, a system of measurement was set up (Fig. 4.9). The set up was placed inside the cryostat. The hole going through the setup is aligned with a hole on the tip where it is placed. A white light source is placed in the back of the cryostat with a lens to focus this light into the desired hole. The light transmitted through the sample is then collected by the monochrometer-PMT system, in order to obtain the position of the C1-HH1 absorption peak.

The samples were placed on a diaphragm which can be moved forward by the force of an electromagnet applying a tensile strain on the samples (Fig. 4.10). Increasing the applied voltage in turn causes an increase in the applied tensile strain.

The structure under investigation was grown on (111)B GaAs and is shown in Fig. 4.11. It has 20 quantum wells made of $In_{0.12}Ga_{0.88}As$/ $Al_{0.15}Ga_{0.85}As$ with a well width of 110 Å, and a barrier width is 200 Å.

The effect of increasing the coil voltage on the C1-HH1 transition for the sample at room temperature and at 13 K is shown in Figs. 4.12-13. It can be seen that this transition moves towards a lower energy suggesting the presence of a tensile strain affecting the sample. This decrease in energy

is accompanied by a reduction in the absorption peak intensity.

The trend is the same for both temperatures but for the measurement done at 13 K the energy shift is larger than that at room temperature (16.4 meV at 300 K, 47.5 meV at 13 K). This can be explained by the fact that the adhesive used to place the sample on the diaphragm (Crazy Glue), shrinks at low temperatures, adding more tension to the sample, moving the C1-HH1 transition higher in energy.

Care was giving to the reduction of the area where the adhesive material makes contact with the sample. It was found that, for 13 K measurement, having a large contact area will completely bleach the C1-HH1 absorption peak.

To learn more about this applied tensile stress, a simulation was run using the modified Kronig-Penney model (including electric field) introduced in Chap 3, to evaluate the amount of compressive strain and electric field remaining in the layers. Figs. 4.14 and 4.15 show the amount of the expected change in the lattice constant and the strain-induced electric field. Increasing the coil voltage will reduce the percentage lattice mismatch and the electric field These values are different for the room temperature and 13 K cases because of the reasons mentioned previously.

The application of a coil voltage of 2 volts will reduce the strain by 0.40% and 0.51%, and the electric field by 6.195×10^4 V cm^{-1} and 8.08×10^4 V cm^{-1}, in the cases of room temperature and 13 K. That is a 47.66% and 46.3% reduction

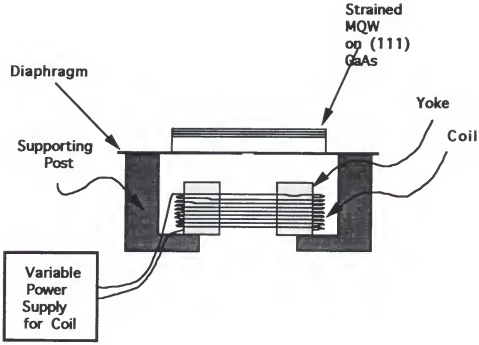

Fig. 4.9 The set up used to apply mechanical strain.

in the strain and the electric field, respectively, for the room temperature, while the reduction is 73.38% and 70.87%, respectively, for the 13 K case.

In conclusion, we have proved the presence of a strain induced electric field in the (111) grown samples by the use of intensity controlled photoluminescence. These same measurements showed no such electric field in (100) grown samples. Then the screening of this electric field was determined from these previous measurements.

Finally, the application of mechanical strain on a (111) grown sample showed a substantial change in the position of C1-HH1 absorption peak under low bias values. This feature can be used to design and operate (111) based switches.

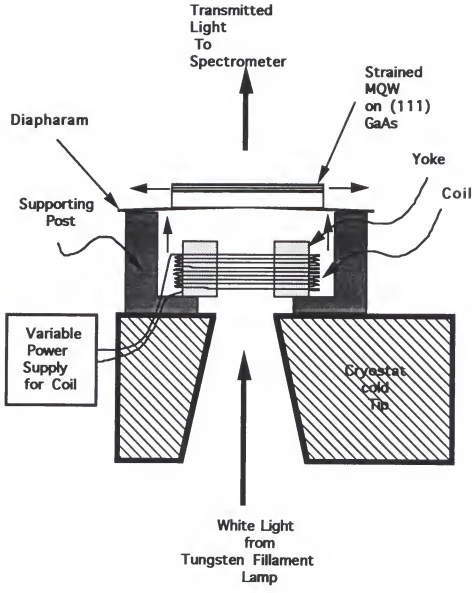

Fig 4.10 Sample under strain.

p+	200 nm	GaAs
p	300 nm	$Al_{0.25}Ga_{0.75}As$
i	700 nm	$Al_{0.15}Ga_{0.85}As$
i	20 prds 20nm $Al_{0.15}Ga_{0.85}As$/110nm $In_{0.12}Ga_{0.88}As$ MQW	
i	700 nm	$Al_{0.15}Ga_{0.85}As$
n	300 nm	$Al_{0.25}Ga_{0.75}As$
n+	500 nm	$Al_{0.25}Ga_{0.75}As$
n+	500 nm	GaAs

(111)B GaAs susbtrate

Fig 4.11 Structure of sample for strain studies.

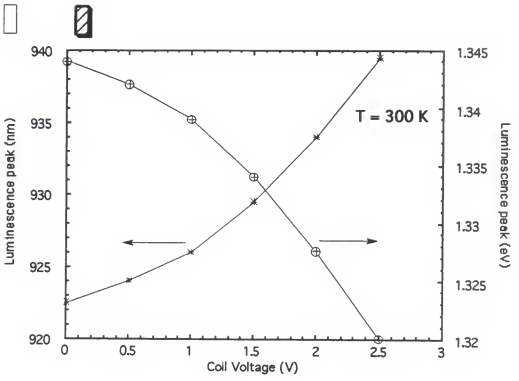

Fig 4.12 Room temperature C1-HH1 absorption peak shift under applied strain.

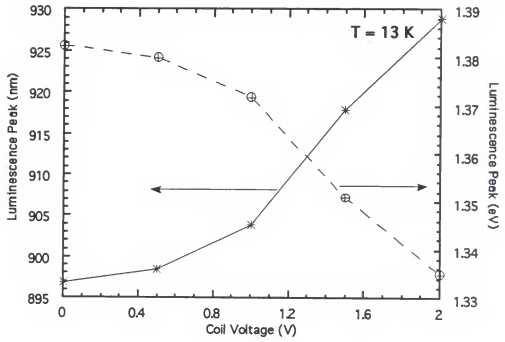

Fig 4.13 13 K C1-HH1 absorption peak shift under applied strain.

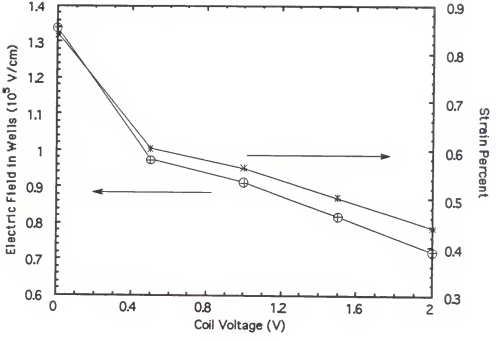

Fig. 4.14 Simulation of effect of applied strain on the built-in electric field and on the strain percentage in the layers at room temperature.

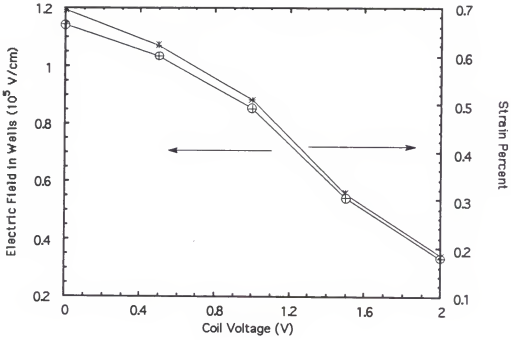

Fig. 4.15 Simulation of effect of applied strain on the built-in electric field and on the strain percentage in the layers at 13 K.

CHAPTER 5
CHARACTERIZATION OF THE THIRD ORDER NONLINEARITY

5.1 Introduction

Intensity dependent nonlinearities have been investigated for AlGaAs/GaAs and strained InGaAs/AlGaAs MQW structures grown on (100) GaAs substrates. Different experiments can be performed to determine the nonlinear refractive index n_2, using the pump and probe method or the hybrid Mach-Zender interferometer method [53-55].

In this chapter we present the values obtained for the nonlinear refractive index n_2 in the structures grown on (100) and (111)B GaAs substrates. A hybrid Mach-Zender interferometer was used to experimentally determine the value of n_2. This work was limited to TE CW measurements at wavelengths of 980 nm and 992.2 nm.

The structures (S1,S2) were designed to insure a single mode slab waveguide operation at the above mentioned wavelengths, where the guided mode peak has a large overlap with the 10 period MQW region.

5.2 Waveguiding Properties of the Structures

5.2.1 Multilayer Matrix Theory

In order to determine the appropriate compositions of the different layers to insure a single mode operation the multilayer matrix method was used [56,57]. This method depends on equating the fields at the boundaries of each layer and deriving the dispersion relation for the total structure.

The theory of multilayer stacks [56,57] defines two field variables U and V given by

$$U = E_y \tag{5.1a}$$

$$V = \omega\mu H_z \tag{5.1b}$$

which describe the transerve variation of the optical field. U and V are the transverse field distribution in a particular layer of constant refractive index n. These definitions are chosen because U(x) and V(x) are quantities that are continuous at the layer boundaries. From the following equations, derived from Maxwell's equations

$$\beta E_y = -\omega\mu H_x \tag{5.2}$$

$$\frac{\partial E_y}{\partial x} = -j\omega\mu H_z \tag{5.3}$$

$$\frac{\partial H_z}{\partial x} + j\beta H_x = -j\omega\varepsilon E_y \tag{5.4}$$

we obtain the relations

$$U' = -j\,V \tag{5.5a}$$

$$V' = j(\beta^2 - n^2\,k^2)U \tag{5.5b}$$

where the prime indicates differentiation with respect to x. Both U and V obey the transverse wave equation

$$\ddot{U} = (\beta^2 - n^2\,k^2)U \tag{5.6}$$

The general solution of the wave equation in this layer is :

$$U = A\exp(-j\kappa x) + B\exp(j\kappa x) \tag{5.7a}$$

$$V = \kappa\,[A\exp(-j\kappa x) - B\exp(j\kappa x)\,] \tag{5.7b}$$

where

$$\kappa^2 = n^2k^2 - \beta^2 \tag{5.8}$$

The A and B constants can be determined from the values $U_0 = U(0)$ and $V_0 = V(0)$ at the input plane $x = 0$ of the layer, so we have

$$A = \frac{1}{2}\left(U_0 + \frac{V_0}{\kappa}\right) \tag{5.9}$$

$$B = \frac{1}{2}\left(U_0 - \frac{V_0}{\kappa}\right) \tag{5.10}$$

A rearrangement of equations (5.7-10) leads to a simple matrix relation between the output quantities U, V and the input quantities U_0 and V_0

$$\begin{pmatrix} U_0 \\ V_0 \end{pmatrix} = \mathbf{M} \begin{pmatrix} U \\ V \end{pmatrix} \tag{5.11}$$

where the pairs (U_0, V_0) and (U, V) have been written as vectors, and $\mathbf{M}$ is the *characteristic matrix* of the layer. This matrix has the form

$$\mathbf{M} = \begin{vmatrix} \cos(\kappa x) & \left(\frac{j}{\kappa}\right)\sin(\kappa x) \\ j\kappa\sin(\kappa x) & \cos(\kappa x) \end{vmatrix} \tag{5.12}$$

Next, consider a stack of n layers sandwiched between substrate and cover as seen in Fig. 5.1. The layers are labeled starting from the substrate. the layer thicknesses are h_i and the layer indices are n_i, where i = 1 to n. The output field variables for each layer are U_i and V_i. The characteristic matrices at the layers are

$$M_i = \begin{vmatrix} \cos(\kappa_i h_i) & \left(\frac{j}{\kappa_i}\right)\sin(\kappa_i h_i) \\ j\kappa_i \sin(\kappa_i h_i) & \cos(\kappa_i h_i) \end{vmatrix} \tag{5.13}$$

where

$$\kappa_i^2 = n_i^2 k^2 - \beta^2 \tag{5.14}$$

The corresponding field variables are related by

$$\begin{pmatrix} U_{i-1} \\ V_{i-1} \end{pmatrix} = M_i \begin{pmatrix} U_i \\ V_i \end{pmatrix} \tag{5.15}$$

Using matrix multiplication, a simple relation between the input variables U_0, V_0 at the substrate and the output variables Un, Vn at the cover can be obtained

$$\begin{pmatrix} U_0 \\ V_0 \end{pmatrix} = M \begin{pmatrix} U_n \\ V_n \end{pmatrix} \tag{5.16}$$

where M is the characteristic matrix of the stack. It is given by the product of the individual layer matrices

$$M = \begin{vmatrix} m_{11} & m_{12} \\ m_{21} & m_{22} \end{vmatrix} = M_1 . M_2 \ldots M_n \tag{5.17}$$

where m_{11}, m_{12}, m_{21} and m_{22} are the matrix elements.

The reflection and transmission coefficients for the light incident on the stack can be determined as follows, Assuming the light is incident from the substrate side, it can described by Eqs. (5.7a) and (5.7b) with

$$\kappa_s^2 = n_s^2 k^2 - \beta^2 = -\gamma_s^2 \tag{5.18}$$

along with the incident amplitude A_s and the reflected amplitude B_s. Therefore, the input variables are

$$U_0 = A_s + B_s \tag{5.19a}$$

$$V_0 = \kappa_s (A_s - B_s) \tag{5.19b}$$

On the cover side, the transmitted light has an amplitude A_c, and the corresponding output variables

$$U_n = A_c \tag{5.20a}$$

$$V_n = \kappa_c A_c \tag{5.20b}$$

where

$$\kappa_c^2 = n_c^2 k^2 - \beta^2 = -\gamma_c^2 \tag{5.21}$$

The optical field in the substrate and the cover layers consist of evanescent waves. The corresponding fields are written in the form

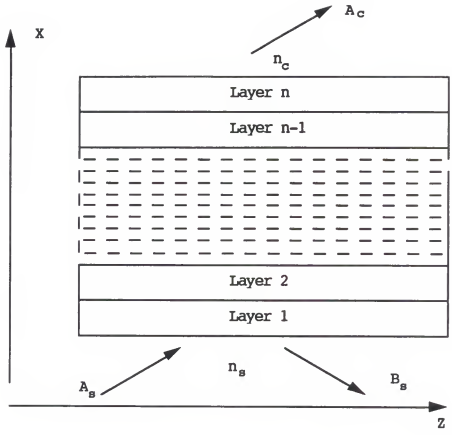

Fig. 5.1 Schematic of n layer stack.

$$U = A \exp(\gamma x) + B \exp(-\gamma x) \tag{5.22}$$

$$V = j\gamma(A \exp(\gamma x) - B \exp(-\gamma x)) \tag{5.23}$$

which obey the transverse wave Eqs. (5.6). Instead of the transverse propagation constants κ_s and κ_c, the transverse decay constants γ_s and γ_c should be used. Considering that the fields should decay away from the multilayer, the input and output field variables are

$$U_0 = A_s \tag{5.24a}$$

$$V_0 = j\gamma_s A_s \tag{5.24b}$$

$$U_n = B_c \tag{5.24c}$$

$$V_n = -j\gamma_c A_c \tag{5.24d}$$

Inserting Eqs. (5.24a-d) into equation 5.16 yields

$$A_s = (m_{11} - j\gamma_c m_{12})B_c \tag{5.25}$$

$$j\gamma_s A_s = (m_{21} - j\gamma_c m_{22})B_c \tag{5.26}$$

Dividing these two relations leads to the dispersion relation for a multilayer slab guide

$$j(\gamma_s m_{11} + \gamma_c m_{22}) = m_{21} - \gamma_s \gamma_c m_{12} \tag{5.27}$$

This relation establishes the connection between the frequency ω of the light and the propagation constant β of the mode guided by the multilayer.

5.2.2 Refractive Index of Different Layers

The refractive index value for GaAs, AlGaAs and InGaAs have been reported earlier [58-60]. These values, at a given wavelength, can be derived by the use of the single-effective-oscillator (SEO) method given by Nahory et al. [60], Utaka et al. [61], and Broberger and Lingren [62]

$$n = \sqrt{1 + \frac{E_d}{E_0} + \frac{E_d}{E_0^3} E^2 + \frac{\eta}{\pi} E^4 \ln\left(\frac{2E_0^2 - E_g^2 - E^2}{E_g^2 - E^2}\right)} \qquad (5.28)$$

Where

$$\eta = \frac{\pi E_d}{2 E_0^2 (E_0^2 - E_g^2)} \qquad (5.29)$$

The parameters E_0, E_d and E_g are expressed in eV by the following empirical relations :

i) For $Al_xGa_{1-x}As$

$$E_0 = 3.65 + 0.871\ x + 0.179\ x^2 \tag{5.30}$$

$$E_d = 36.1 - 2.45\ x \tag{5.31}$$

$$E_g = 1.424 + 1.266\ x + 0.26\ x^2 \tag{5.32}$$

ii) For $In_yGa_{1-y}As$

$$E_0 = 3.65 - 2.15\ y \tag{5.33}$$

$$E_d = 36.1 - 19.9\ y \tag{5.34}$$

$$E_g = 0.36 + 0.505\ (1-y) + 0.555\ (1-y)^2 \tag{5.35}$$

Replacing Eqs. (5.30-32) in equation will yield a value of the refractive index with respect to energy for different values of the Al composition x.

For InGaAs the shift in energy due to lattice mismatch growth would change the refractive index value considerably for high Indium percentage. Das and Bhattacharya [63] has showed a decrease in the refractive index of InGaAs/GaAs heterostructures due to the increase in the bandgap of InGaAs material under compressive strain. For our samples the value of the Indium percentage (10% in S1, 5% in S2) is too small so this effect is not present. The refractive index of GaAs, $Al_{0.2}Ga_{0.8}As$, and $In_{0.05}Ga_{0.95}As$ are presented in Fig. 5.2.

The refractive index of the MQW, given by Glick and Reinhart [64], is derived from

$$n_{||MQW} = \sqrt{\frac{L_b\, n^2_{AlGaAs} + L_z\, n^2_{InGaAs}}{L_b + L_z}} \tag{5.36}$$

Using the determined values of the refractive indices in the equations derived from the multilayer matrix theory described above, the modefield can be obtained. These modefields are shown in Figs. 5.3 to 5.6 for the TE_0 mode. In these figures the position zero corresponds to the bottom of the QW region. It can be seen that the field's peak is within the MQW region.

5.3 Nonlinearities in Proposed Structures

5.3.1 Introduction

A linear dielectric medium is characterized by a linear relation between the polarization density and the electric field, $\mathbf{P} = \varepsilon_0 \chi \mathbf{E}$, where ε_0 is the permitivity of free space and χ is the electric susceptibility of the medium. A nonlinear dielectric medium, on the other hand, is characterized by a nonlinear relation between **P** and **E**.

Since externally applied optical electric fields are typically small in comparison with characteristic interatomic or crystalline fields, the nonlinear term is usually weak.

The relation between **P** and **E** is then approximately linear for small **E**, deviating only slightly from linearity as **E** increases. Under these circumstances, it is possible to expand the function that relates **P** to **E** in a Taylor's series about **E** = 0,

$$\mathbf{P} = a_1\mathbf{E} + \frac{1}{2}a_2\mathbf{E}^2 + \frac{1}{6}a_3\mathbf{E}^3 + \ldots \tag{5.37}$$

The coefficients a1, a2, and a3 are the first, second, and third derivatives of P with respect to E at E = 0. The first term, which is linear, dominates at small E. The second term represents a quadratic or second-order nonlinearity, the third term represents a third order nonlinearity, and so on.

The above equation is usually written as [65]

$$\mathbf{P} = \varepsilon_0\chi\,\mathbf{E} + 2d\,\mathbf{E}^2 + 4\chi^{(3)}\,\mathbf{E}^3 + \ldots \tag{5.38}$$

In media possessing centrosymmetry, the second-order term is absent since the polarization must reverse exactly when the electric field is reversed. The dominant nonlinearity is then of third order,

$$\mathbf{P}_{NL} = 4\chi^{(3)}\,\mathbf{E}^3 \tag{5.39}$$

A material with large third order nonlinearity is sometimes called a Kerr medium.

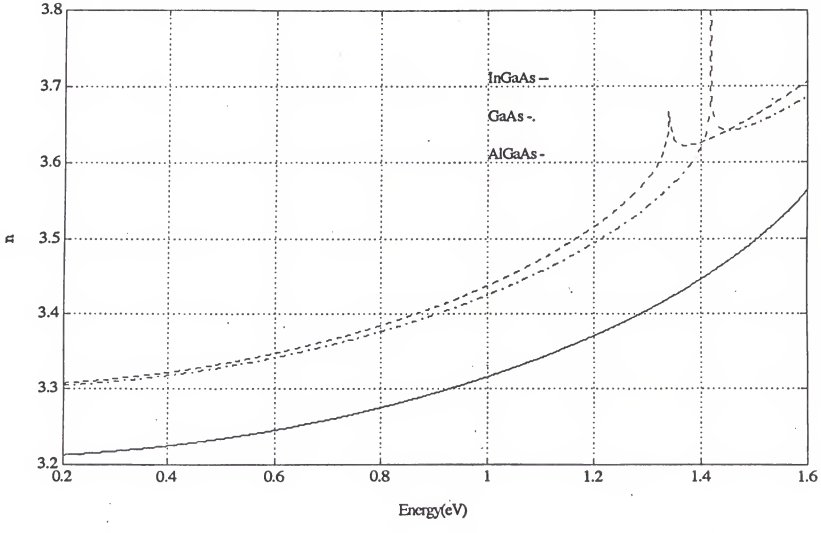

Fig. 5.2. The refractive index vs. Energy for GaAs, $Al_{0.2}Ga_{0.8}As$, and $In_{0.05}Ga_{0.95}As$.

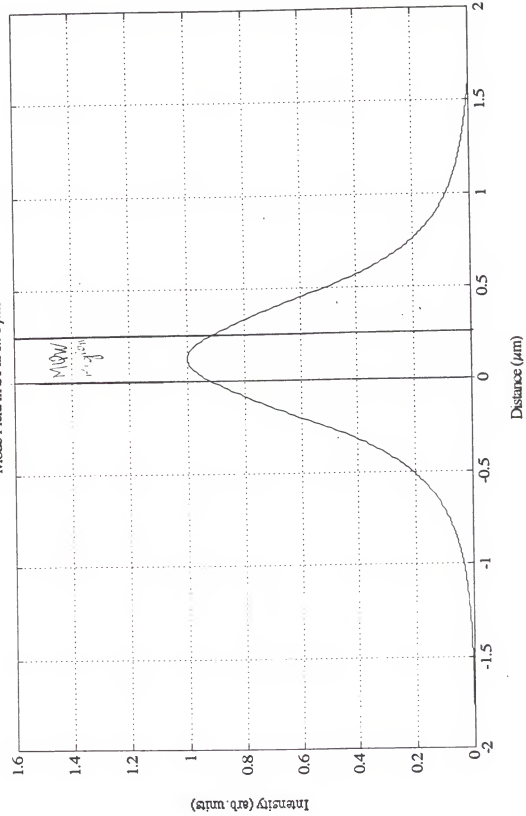

Fig. 5.3. The modefield for the structure S1 at λ_0 = 980 nm.

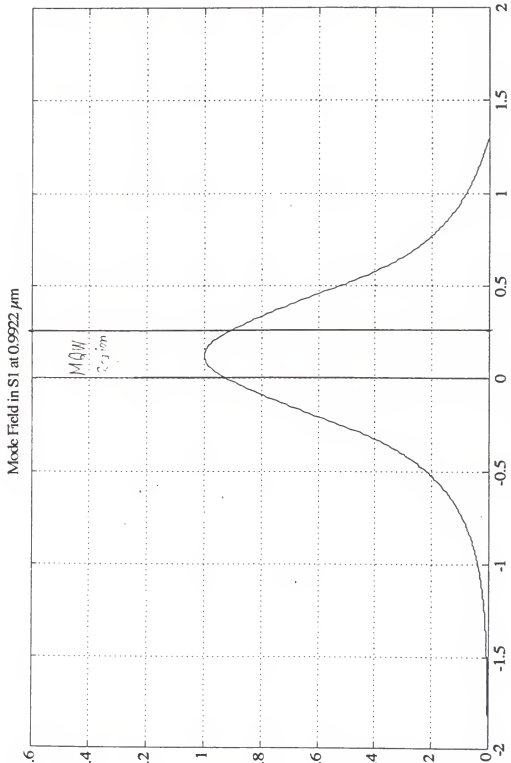

Fig. 5.4. The modefield for the structure S1 at λ_o = 992.2 nm.

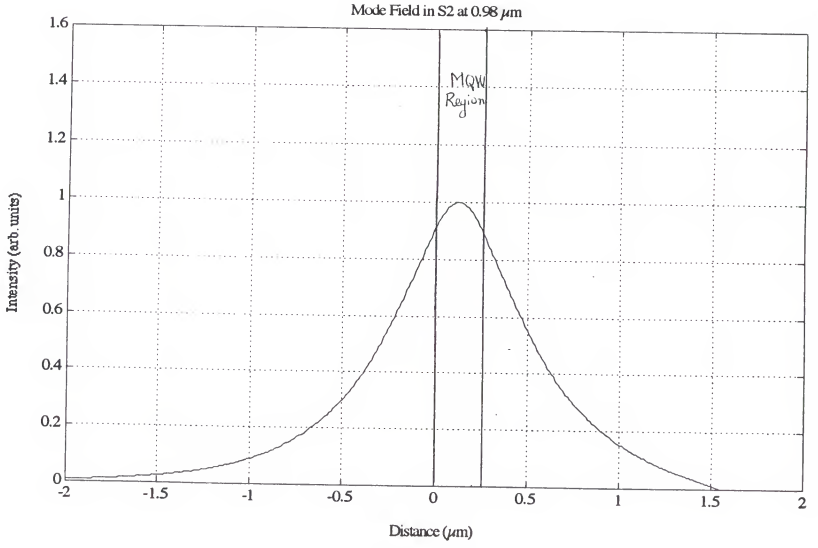

Fig. 5.5. The modefield for the structure S2 at λ_o = 980 nm.

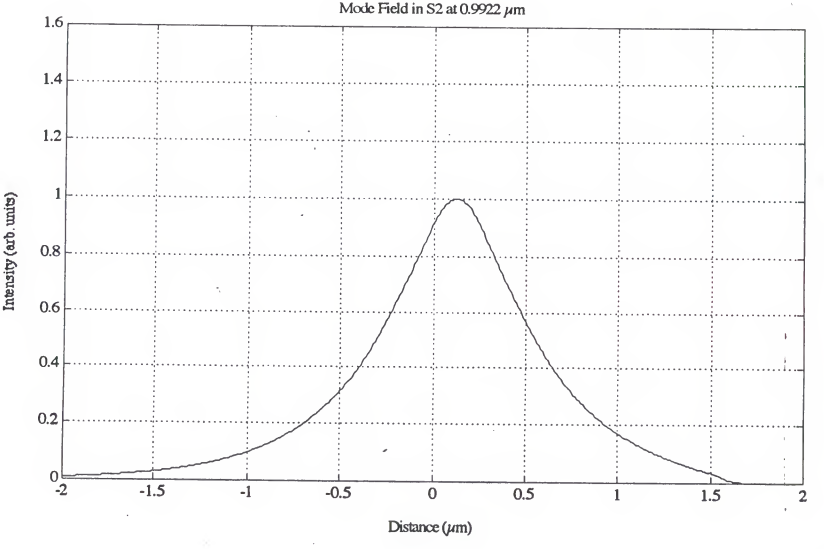

Fig. 5.6. The modefield for the structure S2 at λ_o = 992.2 nm.

In accordance with Eq. 5.39, the response of a third-order nonlinear medium to a monochromatic optical field $\mathbf{E}(t) = \mathrm{Re}\{E(\omega)\exp(j\omega t)\}$ is nonlinear polarization $P_{NL}(t)$ containing a component at frequency ω and another at frequency 3ω,

$$P_{NL}(\omega) = 3\chi^{(3)} \mid E(\omega) \mid^2 E(\omega) \tag{5.40}$$

$$P_{NL}(3\omega) = \chi^{(3)} E^3(\omega) \tag{5.41}$$

The polarization component at frequency ω in Eq. 5.40 corresponds to an incremental change of the susceptibility $\Delta\chi$ at frequency ω given by

$$\varepsilon_0 \Delta\chi = \frac{P_{NL}(\omega)}{E(\omega)} = 3\chi^{(3)} \mid E(\omega) \mid^2 = 6\chi^{(3)}\eta I \tag{5.42}$$

where $I = \dfrac{\mid E(\omega) \mid^2}{2\eta}$ is the optical intensity of the initial wave. Since $n^2 = 1 + \chi$, this is equivalent to an incremental refractive index $\Delta n = \left(\dfrac{\partial n}{\partial \chi}\right)\Delta\chi = \dfrac{\Delta\chi}{2n}$, so that

$$\Delta n = \frac{3\eta}{\varepsilon_0 n}\chi^{(3)} I = n_2 I \tag{5.43}$$

Thus the third order nonlinearity causes a change in the refractive index proportional to the optical intensity. The overall refractive index is therefore a linear function of the optical intensity I,

$$n(I) = n + n_2 I \tag{5.44}$$

where

$$n_2 = \frac{3\eta_0}{\varepsilon_0 n^2}\,\chi^{(3)} \tag{5.45}$$

is called the nonlinear refractive index.
This effect is known as the optical Kerr effect. This effect is self-induced in that the phase velocity of the wave depends on the wave's own intensity.

5.3.2 Measurements of the Nonlinear Refractive Index

Consider a waveguide where an optical field is launched. Assuming a linear dependence of the phase shift on the input power [55], one can express the value of n_2 as

$$n_2 = \frac{\Delta\phi}{P_i}\left[\frac{2\pi}{\lambda_o A}\left\langle\frac{1-\exp(-\alpha l_z)}{\alpha}\right\rangle\right]^{-1} \tag{5.46}$$

where $\Delta\phi$ is the relative phase shift, P_i is the input power, A is the guide cross section, l_z is the length of the waveguide, λ_o is the free-space wavelength of the incident light, and α is the loss coefficient of the waveguide. Thues, by measuring the phase shift $\Delta\phi$ and the loss coefficient α, the value of n_2 can be determined.

The Mach-Zender interferometer is shown in Fig. 5.7, with the 2mm long waveguides placed in one of the arms. The interference fringes produced due to the difference in the optical path length between the two arms of the Mach-Zender are captured on a computer using a CCD camera and a Frame Grabber Card. Increasing the input power causes a shift in the interference pattern (Fig. 5.8). The peaks in Fig. 5.8 correspond to the bright areas in the interference pattern, while the valleys correspond to the dark areas. The phase difference corresponding to two consecutive peaks (valleys) is 180 degrees. From that we can calculate the phase shift $\Delta\phi$ with power when displaying the interference pattern for two power values. The phase shift with the increase of input power is presented in Figs.5.9 and 5.10 for all four samples at λ_o = 980 and 992.2 nm. It can be seen that S1 (111) sample shows a leveling off at high optical powers suggesting a high optical powers suggesting a saturation of the nonlinearity.

The value of α for each of the samples was obtained by the cut back method. The estimated values of n_2 for different powers, for wavelengths of 980 and 992.2 nm, for all the samples are given in Table 5.1 and 5.2. The values of n_2 obtained for the (100) grown samples are comparable to those reported in refs. [9,66,67]. These data show that the (111) grown samples have 30-50% higher nonlinear refractive index compared to their (100) grown counterparts.

The origin of n_2 can be thermal or electronic. For CW measurements both of them are present, while in pulsed measurements, with pulse duration less than 10 ns, the origin of n_2 is mainly electronic. The thermal effect moves the transition energies of the MQWs to lower values increasing the samples' refractive index (n_2 is positive). On the other hand, the electronic effect will yield an increase in the value of the transition energies, decreasing the refractive index (n_2 is negative).

The transition energy for S1 (100) is from Fig. (3.9) is 1.3716 eV, while for S1(111) it is 1.3974 eV. For S2(100) the value is 1.4019 eV, and for S2(111) it is 1.4298 eV. For λ_o = 980 nm (1.2653 eV), the energy difference between the laser and the closest C1-HH1 transition is 106.29 meV (farthest is 164.5 meV), while for λ_o = 992.2 nm (1.2497 eV) the closest becomes 121.85 meV, while the farthest will be 180 meV. For sources operating so far from the transition energies, the thermal effect is not large, owing the origin of the nonlinearity to the electronic effect(n_2 is negative).

For (100) samples only the electronic effect is present, while for the (111) grown samples there is an additional factor influencing the value of n_2. That factor is the screening of the strain-induced electric field increasing the value of n_2.

The value of n_2 is closely connected to that of α, increasing α would increase n_2. Eventhough the (100) samples are closer in energy to the energy of the lasers used in this

experiment, the value of α is higher in the (111) samples. This is probably due to the dispersion along the layers interfaces in these samples.

The values of n_2, for (100) samples, reported here are comparable to values given by others [63]. The decrease in the value of n_2 between $\lambda_o = 980$ and 992.2 nm can explained by the reduction of the absorption coefficient when operating farther away from the band edge. This trend was observed by other researchers doing wavelength dependent measurements of n_2[68].

Furthermore, Moise et al. [67] using time-resolved photoluminescence measurements of similar p-i-n structures grown on (100) and (111) substrates with a single InGaAs/AlGaAs quantum well in the i region, showed that the (111) grown sample exhibited a smaller luminescence decay time than the (100) grown sample in response to an increase in photogenerated carrier density (1.625 times shorter). This shows that future pulsed measurements may demonstrate much better performance of (111) strained MQWs nonlinearities than that of the (100) grown MQWs.

The figure of merit for the (100) and (111) samples is given by

$$F = \frac{n_2}{\tau\alpha} \tag{5.47}$$

where τ is the decay time.

so,

$$\frac{F_{(111)}}{F_{(100)}} = \frac{n_{2(111)}\tau_{(100)}\alpha_{(100)}}{n_{2(100)}\tau_{(111)}\alpha_{(111)}} \qquad (5.48)$$

for S1,

$$\frac{F_{(111)}}{F_{(100)}} = 1.69 \qquad (5.49)$$

and for S2,

$$\frac{F_{(111)}}{F_{(100)}} = 0.926 \qquad (5.50)$$

The 70% improvement in the figure of merit value in the case of S1 (10%) makes the (111)B grown strained MQWs with a high In percentage a better choice for the design and fabrication of nonlinear switches. While for S2(5% In) the figure seems to be the same, showing that the screening effect here does not play as a bigger role.

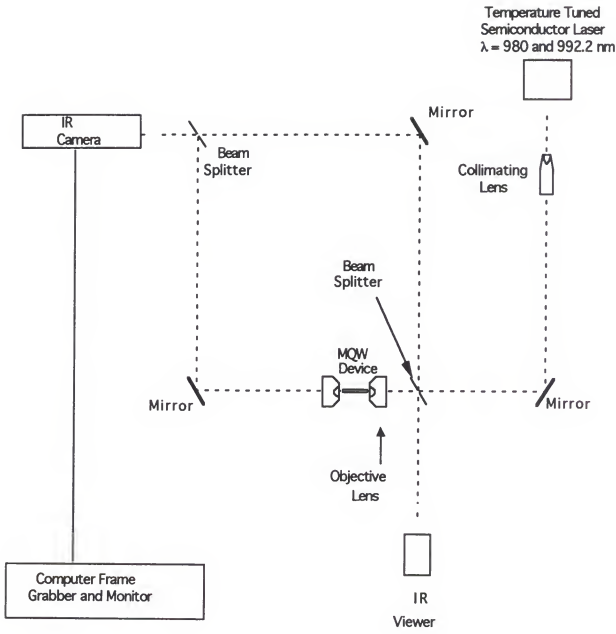

Fig 5.7. The Mach-Zender interferometer setup.

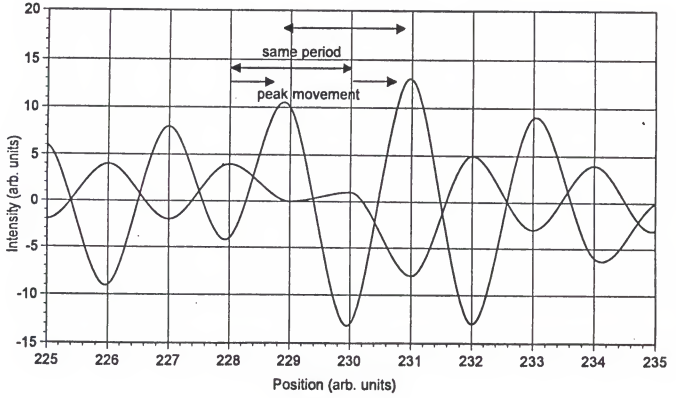

Fig. 5.8. The shift in interference pattern with increase of input laser power.

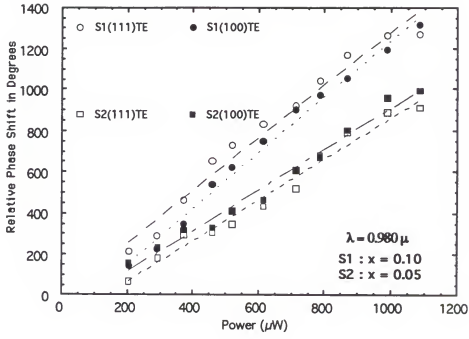

Fig. 5.9. Relative phase shift with increase in input power for λ_o = 980 nm.

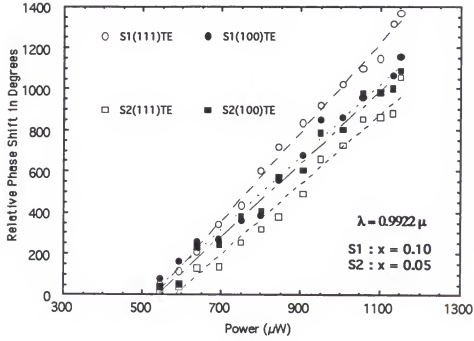

Fig. 5.10. Relative phase shift with increase in input power for λ_o = 992.2 nm.

Table 5.1 n_2 for λ_o = 980 nm

TE $\lambda = 0.980\ \mu m$	Length (cm)	Loss Coefficient α (cm^{-1})	n_2 (cm^2/W)
S1(111)	0.200	7.3	$8.69\ 10^{-8}$
S1(100)	0.225	5.7	$6.55\ 10^{-8}$
S2(111)	0.200	4.3	$4.83\ 10^{-8}$
S2(100)	0.250	1.5	$3.05\ 10^{-8}$

Table 5.2 n_2 for λ_o = 992.2 nm

TE $\lambda = 0.9922\ \mu m$	Length (cm)	Loss Coefficient α (cm^{-1})	n_2 (cm^2/W)
S1(111)	0.200	1.5	$3.52\ 10^{-8}$
S1(100)	0.225	1.2	$2.65\ 10^{-8}$
S2(111)	0.200	0.9	$2.64\ 10^{-8}$
S2(100)	0.250	0.3	$1.70\ 0^{-8}$

CHAPTER 6
CONCLUSIONS AND RECOMMENDATIONS

The study of the proposed structures grown on (111)B GaAs yielded some important features. The first of which is the proof of the existence of a strain-induced electric field in the strained wells using photoluminescence measurement. This comes from the fact that increasing the optical excitation intensity used to test the samples would increase the e-h pairs created in the wells. Since the presence of an electric field in the wells would cause a red shift (QCSE) in the transition energies, the e-h pairs would act to screen any existing built-in electric field reducing the effect that such field has on the transitions energies. That means, under increased excitation the transitions energies should move to higher values. That is what was observed in the PL spectra for (111)B grown samples, while this trend was absent in the (100) grown samples.

The subjection of a (111) grown sample to mechanical tension showed a shift in the excitonic absorption peak of the MQW to lower energies, depending on how much pressure was introduced. We showed that an application of a low bias would produce a shift of 24 meV at 300 K, and 53 meV at 13 K. This discrepancy in the value of shift between the two

temperatures is probably due to the added tension because of the shrinkage of the adhesive used to place the sample on the test setup. Since the application of strain can produce a shift in the absorption peak , this feature can be used to operate this sample as an electrically controlled switch.

Finally, the value of the nonlinear refractive index was measured, with the help of a hybrid Mach-Zender interferometer setup, using CW TE lasers operating at 980 and 992.2 nm. The 980 nm operating laser is 112 meV and 140 meV below the C1-HH1 transitions of samples S1 and S2, respectively, while for the 992.2 nm laser this separation is 127 meV and 167 meV, respectively.

The relative phase shift of the interference pattern due to the increase of optical radiation was recorded, and the loss coefficient was measured by the cut-back method. These measurements yielded a higher value of n_2 for (111) samples compared with the (100) samples. The figure of merit was 70% higher for S1(111) than S1(100), such improvement was not present for the S2 samples, probably because the screening effect does not play an important role in the latter case.

Because of the lack of equipment, it was not feasible to perform this same experiment with pulsed laser sources in order to determine only the electronic part of the nonlinear refractive index. Eliminating thermal effects, we expect this value to be higher also in the case of (111) grown structures. This can be explained by the fact that there are two factors contributing to the increase in the value of

$n_{2electronic}$(the sign of which is negative). These factors are the electronic effect working to increase the bandgap reducing the refractive index, and the screening of the strain-induced electric field which has the same effect on the refractive index. While the first factor is present in (100) grown structures, the second effect is completely absent.

This research showed that the (111) grown with a high In percentage (10%) should be a better choice than their (100) counterparts when used in the design and operation of nonlinear-based optical devices.

APPENDIX A
CALCULATION OF THE C1-HH1&LH1
TRANSITION ENERGIES IN (100) SAMPLES

The calculation of the value of the C1-HH1,LH1 transition in the InGaAs/AlGaAs MQWs is performed using the Kronig-Penney model. The effect of strain on these transitions is also included.

For the case of an infinite periodic one-dimensional square-well potential (Fig. A.1) it is possible to arrive at an exact solution of the Schr ödinger equation. Kronig and Penney investigated the solution, and although it is related to a somewhat idealized periodic potential which is only a crude approximation to that found in the actual crystal, it is nevertheless very useful because it serves to illustrate in a most explicit way many of the important characteristic features of the quantum behavior of electrons in periodic lattices. The wave equation associated with this model may be calculated in the one-electron approximation by solving Schrödinger's equation

$$\frac{d^2\psi}{dx^2} + \frac{2m}{\hbar^2}\left(E-V(x)\psi(x)\right) = 0 \qquad (A.1)$$

for a single electron in the periodic potential V(x). Since the wave functions must have the Bloch form, it is expected that

$$\psi(x) = e^{ikx}\, u(x) \tag{A.2}$$

Substituting Eq. A.2 in Eq. A.1, it is found that the function u(x) must satisfy

$$\frac{d^2u}{dx^2} + 2ik\,\frac{du}{dx} - \left(k^2 - \alpha^2 + \frac{2mV(x)}{\hbar^2}\right) u(x) = 0 \tag{A.3}$$

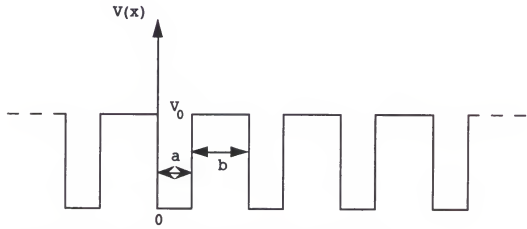

Fig. A.1 Ideal periodic square well potential.

where

$$\alpha = \sqrt{\frac{2mE}{\hbar^2}} \tag{A.4}$$

For the potential in Fig. A.1, it is found that

$$\frac{d^2u_1}{dx^2} + 2ik\frac{du_1}{dx} - \left(k^2 - \alpha^2\right) u_1(x) = 0 \quad (0 < x < a) \tag{A.5}$$

$$\frac{d^2u_2}{dx^2} + 2ik\frac{du_2}{dx} - \left(k^2 - \beta^2\right) u_2(x) = 0 \quad (-b < x < 0) \tag{A.6}$$

where $u_1(x)$ represents the value of $u(x)$ in the interval $(0<x<a)$ and $u_2(x)$ represnts the value of $u(x)$ in $(-b<x<0)$, and where β is an imaginary value expressed by

$$\beta = \sqrt{\frac{2m(E-V_0)}{\hbar^2}} \tag{A.7}$$

The solution for these differential equations are

$$u_1(x) = A\, e^{i(\alpha-k)x} + B\, e^{-i(\alpha+k)x} \qquad (0<x<a) \tag{A.8}$$

$$u_2(x) = C\, e^{i(\beta-k)x} + D\, e^{-i(\beta+k)x} \qquad (-b<x<0) \tag{A.9}$$

where A, B, C, and D are arbitrary constants.

The requirement of continuity for the wave function and its derivative at x = a and x = -b demands that the functions $u(x)$ satisfy the same conditions. Using these boundary conditions, the resulting equation is

$$\frac{\gamma^2 - \alpha^2}{2\alpha\gamma} \sinh(\gamma b) \sin(\alpha a) + \cosh(\gamma b) \cos(\alpha a) = \cos k(a+b) \tag{A.10}$$

where

$$\beta = i\gamma \tag{A.11}$$

Solving Eq.A.10 will yield the energy values of the needed transitions.

Furthermore, the application of biaxial stress in the plane of growth can be pictured as a hydrostatic stress and a uniaxial stress along the direction perpendicular to the growth plane. The hydrostatic component shifts the center of gravity of the J = 3/2 multiplet and the J = 1/2 multiplet relative to the conduction band. The uniaxial strain component splits the normally degenerate J = 3/2, m_j = 1/2 and J = 3/2, m_j = 3/2 valence band edges. For layers under compression, m_j = 3/2 holes become heavy in the growth direction, and light in the layer plane, and vice-versa for the m_j = 1/2 holes.

With the superposition of the hydrostatic and uniaxial stress components, shifts in the bandgap can be writen as

$$\Delta E_0(1) = \left[-2\ a \left(\frac{C_{11} - C_{12}}{C_{11}}\right) + b \left(\frac{C_{11} + 2\ C_{12}}{C_{11}}\right)\right] \varepsilon \tag{A.12}$$

$$\Delta E_0(2) = \left[-2\ a \left(\frac{C_{11} - C_{12}}{C_{11}}\right) - b \left(\frac{C_{11} + 2\ C_{12}}{C_{11}}\right)\right] \varepsilon \tag{A.13}$$

Where $\Delta E_0(1)$, $\Delta E_0(2)$ ar the shifts of the heavy hole, and the light hole valence bands, respectively. ε is the biaxial strain parallel to [100] and [010] directions, taken here to be the mismatch Δa, a and b are the hydrostatic and the shear deformation potentials, respectively.

The values of a, b, C11 and C12 for different $In_xGa_{1-x}As$ compositions are calculated by interpolating the binary values for GaAs and InAs, using Vegard's law.

Program to Calculate the C1-HH1,LH1
Transition Energy
In (100) Grown Samples

```
***** Deriving the Parameters of AlGaAs an InGaAs *****
clc
clear
M=9.1095e-31;
x=0.1;
y=0.2;
i=1;
j=1;
k=1;
hb1 = 6.58219e-16;
hb2 = 1.05459e-34;

aGaAs = 5.6533;
aInAs = 6.0584;
aAlAs = 5.6611;
aInGaAs = x*aInAs +(1-x)*aGaAs;
aAlGaAs = y*aAlAs +(1-y)*aGaAs;

C11GaAs = 11.88;
C12GaAs = 5.38;

C11InAs = 8.329;
C12InAs = 4.526;
```

```
C11InGaAs = x*C11InAs + (1-x)*C11GaAs;
C12InGaAs = x*C12InAs + (1-x)*C12GaAs;

AGaAs = -9.8;
AInAs = -5;
BGaAs = -1.76;
BInAs = -1.8;

AInGaAs = x*AInAs +(1-x)*AGaAs;
BInGaAs = x*BInAs +(1-x)*BGaAs;

EgInGaAs = 0.36 + 0.505 *(1-x) + 0.555*((1-x)^2)
EgAlGaAs = 1.424 + 1.266 * y + 0.26 *(y^2);

mcInGaAs = M*(x*0.023 + (1-x)*0.067);
mcAlGaAs = M*(0.0665 + 0.0835 * y);

mhhInGaAs = M*(x*0.34+(1-x)*0.92);
mhhAlGaAs = M*(y*0.4+(1-y)*0.35);

mlhInGaAs = M*(x*0.027 + (1-x)*0.08);
mlhAlGaAs = M*(0.18*y + (1-y)*0.08);

***** The Energy Shift Due to Strain *****

Δa = (aInGaAs-aAlGaAs)/aAlGaAs;
dEhh1 = -2*AInGaAs*((C11InGaAs-C12InGaAs)/C11InGaAs);
```

```
dEhh2 = BInGaAs*((C11InGaAs+2*C12InGaAs)/C11InGaAs);
dEhh = (dEhh1 + dEhh2)* Δa;

dElh1 = -2*AInGaAs*((C11InGaAs-C12InGaAs)/C11InGaAs);
dElh2 = -BInGaAs*((C11InGaAs+2*C12InGaAs)/C11InGaAs);
dElh = (dElh1 + dElh2)* Δa;

***** Kronig-Penney Model *****

lb=150e-10;
lz=100e-10;

Ee = hb1*hb2*((pi/(lz+27.5e-10))^2)/(2*mcInGaAs)
Evh = hb1*hb2*((pi/(lz+1.5E-10))^2)/(2*mhhInGaAs)

dEv = 0.4 * (1.247*y + 1.5*x - 0.4*(x^2));
dEc = 0.6 * (1.247*y + 1.5*x - 0.4*(x^2));

Ec = zeros(1,2000);
Evhh = zeros(1,2000);
Evlh = zeros(1,2000);

for E=1e-3:1e-3:dEv
alpha1=sqrt(2*E*mcInGaAs/(hb1*hb2));
gamma1=sqrt(2*(dEc-E)*mcAlGaAs/(hb1*hb2));

r1= ((gamma1)^2-(alpha1)^2)/(2*alpha1*gamma1);
```

```
r2 = (sinh(gamma1*lb)*sin(alpha1*lz));
r3 = (cosh(gamma1*lb)*cos(alpha1*lz));
r=r1*r2+r3;

if sign(r)<=0
Ec(1,i)=E;
i=i+1;
end

alpha2=sqrt(2*E*mhhInGaAs/(hb1*hb2));
gamma2=sqrt(2*(dEv-E)*mhhAlGaAs/(hb1*hb2));


t1= ((gamma2)^2-(alpha2)^2)/(2*alpha2*gamma2);
t2 = (sinh(gamma2*lb)*sin(alpha2*lz));
t3 = (cosh(gamma2*lb)*cos(alpha2*lz));
t=t1*t2+t3;

if sign(t)<=0
Evhh(1,j)=E;
j=j+1;
end

alpha3=sqrt(2*E*mlhInGaAs/(hb1*hb2));
gamma3=sqrt(2*(dEv-E)*mlhAlGaAs/(hb1*hb2));

s1= ((gamma3)^2-(alpha3)^2)/(2*alpha3*gamma3);
```

```
s2 = (sinh(gamma3*lb)*sin(alpha3*lz));
s3 = (cosh(gamma3*lb)*cos(alpha3*lz));
s=s1*s2+s3;

if sign(s)<0
Evlh(1,k)=E;
k=k+1;
end

end


***** C1-HH1 and C1-LH1 Transition Energies *****

E11h = EgInGaAs + Ec(1,1) + Evhh(1,1);
E11l = EgInGaAs + Ec(1,1) + Evlh(1,1);

E11h = E11h + dEhh
E11l = E11l + dElh
E11hw = 1.24/E11h
E11lw = 1.24/E11l
Ec(1,1)
Evhh(1,1)
```

APPENDIX B
CALCULATION OF THE C1-HH1&LH1 TRANSITION ENERGIES IN (111) SAMPLES

The calculation of the value of the C1-HH1,LH1 transition in the InGaAs/AlGaAs MQWs is done using the Kronig-Penney model. The effect that strain has on these transitions is also included. In the case of (111) grown layers, the energy shift due to strain is larger than that in the (100) counterparts. Furthermore, the presence of a strain-induced electric field in the strained layers would reduce the transitions energies. These different factors are incorporated in the following program to calculate the values of the needed transitions.

Program to Calculate the C1-HH1,LH1
Transition Energy
In (111) Grown Samples

***** Deriving the Parameters of AlGaAs an InGaAs *****

```
clc
clear

M=9.1095e-31;
x=0.1;
y=0.15;
i=1;
j=1;
k=1;
hb1 = 6.58219e-16;
hb2 = 1.05459e-34;
aGaAs = 5.6533;
aInAs = 6.0584;
aAlAs = 5.6611;
aInGaAs = x*aInAs +(1-x)*aGaAs;
aAlGaAs = y*aAlAs +(1-y)*aGaAs;
o = (aInGaAs-aAlGaAs)/aAlGaAs;
fa=0;
fb=0;

eGaAs = 13.1;
eAlAs = 10.1;
```

```
eInAs = 15.15;
eAlGaAs = y*eAlAs + (1-y)*eGaAs;
eInGaAs = x * eInAs + (1 - x) * eGaAs;
e14GaAs = -.16;
e14InAs = -.045;
e14InGaAs = x * e14InAs + (1 - x) * e14GaAs;

C11GaAs = 11.88;
C12GaAs = 5.38;

C11InAs = 8.329;
C12InAs = 4.526;

C44GaAs = 5.92;
C44InAs = 3.96;

C11InGaAs = x*C11InAs + (1-x)*C11GaAs;
C12InGaAs = x*C12InAs + (1-x)*C12GaAs;
C44InGaAs = x * C44InAs + (1 - x) * C44GaAs;

AGaAs = -9.8;
AInAs = -5;
BGaAs = -1.76;
BInAs = -1.8;

AInGaAs = x*AInAs +(1-x)*AGaAs;
BInGaAs = x*BInAs +(1-x)*BGaAs;
```

```
acGaAs = -18.3;
acInAs = -11.7;
avGaAs = -4.8;
avInAs = -5.2;
dGaAs = -4.4;
dInAs = -4.6;

acInGaAs = x*acInAs +(1-x)*acGaAs;
avInGaAs = x*avInAs +(1-x)*avGaAs;
dInGaAs = x*dInAs +(1-x)*dGaAs;

mcInGaAs = M*(x*0.023 + (1-x)*0.067);
mcAlGaAs = M*(0.0665 + 0.083 * y);

mhhInGaAs = M*0.92;
mhhAlGaAs = M*(1.11*y+0.92*(1-y));

mlhInGaAs = M*(x*0.026 + (1-x)*0.07);
mlhAlGaAs = M*(0.14*y + (1-y)*0.07);

EgInGaAs = 0.36 + 0.505 *(1-x) + 0.555*((1-x)^2);
EgAlGaAs = 1.424 + 1.266 * y + 0.26 *(y^2);

Ee = hb1*hb2*((pi/(lz+27.5e-10))^2)/(2*mcInGaAs);
Evh = hb1*hb2*((pi/(lz+1.5E-10))^2)/(2*mhhInGaAs);
```

```
dEv = 0.4 * (1.247*y + 1.5*x - 0.4*(x^2));
dEc = 0.6 * (1.247*y + 1.5*x - 0.4*(x^2));

Ec = zeros(1,2000);
Evhh = zeros(1,2000);
Evlh = zeros(1,2000);


***** Amount of Electric Field Inside the MQW Region *****

Aa = (C11InGaAs+ 2 * C12InGaAs) / (4 * C44InGaAs);
Ab = (C11GaAs + 2 * C12GaAs) / (4 * C44GaAs);
B = (C11InGaAs + 2 * C12InGaAs) / (C11GaAs + 2 * C12GaAs);

exxa = ((aGaAs / (aInGaAs)) - 1) / ((1 + Aa) + ((1 + Ab) * B
* (lz        / lb)));
exxb = -(lz / lb) * B * exxa;
exya = -2 * Aa * exxa;
exyb = -2 * Ab * exxb;

fa= 2 * exya * e14InGaAs / (8.8542E-12 * eInGaAs)

fb= 2 * exyb * e14GaAs / (8.8542E-12 * eAlGaAs);
```

```
***** The Energy Shift Due to Strain *****

DeltaEc = 3*acInGaAs*exxa;
DeltaEhh = 3*avInGaAs*exxa + 1.73205*dInGaAs*exya;
DeltaElh = 3*avInGaAs*exxa - 1.73205*dInGaAs*exya;



***** Kronig-Penney Model *****

lb=178e-10;
lz=80e-10

for E=1e-3:1e-3:dEv
alpha1=sqrt(2*E*mcInGaAs/(hb1*hb2));
gamma1=sqrt(2*(dEc-E)*mcAlGaAs/(hb1*hb2));

r1= ((gamma1)^2-(alpha1)^2)/(2*alpha1*gamma1);
r2 = (sinh(gamma1*lb)*sin(alpha1*lz));
r3 = (cosh(gamma1*lb)*cos(alpha1*lz));
r=r1*r2+r3;

if sign(r)<=0
Ec(1,i)=E;
i=i+1;
end
```

```
alpha2=sqrt(2*E*mhhInGaAs/(hb1*hb2));
gamma2=sqrt(2*(dEv-E)*mhhAlGaAs/(hb1*hb2));


t1= ((gamma2)^2-(alpha2)^2)/(2*alpha2*gamma2);
t2 = (sinh(gamma2*lb)*sin(alpha2*lz));
t3 = (cosh(gamma2*lb)*cos(alpha2*lz));
t=t1*t2+t3;

if sign(t)<=0
Evhh(1,j)=E;
j=j+1;
end

alpha3=sqrt(2*E*mlhInGaAs/(hb1*hb2));
gamma3=sqrt(2*(dEv-E)*mlhAlGaAs/(hb1*hb2));

s1= ((gamma3)^2-(alpha3)^2)/(2*alpha3*gamma3);
s2 = (sinh(gamma3*lb)*sin(alpha3*lz));
s3 = (cosh(gamma3*lb)*cos(alpha3*lz));
s=s1*s2+s3;

if sign(s)<0
Evlh(1,k)=E;
k=k+1;
end
end
```

```
***** Electric Field Effect on C1-HH1,LH1 Transitions *****

Lzc = 6.626e-34*.5/(sqrt(2*mcInGaAs*Ec(1,1)*1.6e-19));
Lzhh = 6.626e-34*.5/(sqrt(2*mhhInGaAs*Evhh(1,1)*1.6e-19));
Lzlh = 6.626e-34*.5/(sqrt(2*mlhInGaAs*Evlh(1,1)*1.6e-19));

F1c = Ec(1,1)/Lzc;
F1hh = Evhh(1,1)/Lzhh;
F1lh = Evlh(1,1)/Lzlh;

fc = abs(fa/F1c);
fvhh = abs(fa/F1hh);
fvlh = abs(fa/F1lh);

Wc=Ec(1,1)*(0.99969+0.0144*fc-0.014364*(fc^2)+0.00042568
*(fc^3)-
   5.58e-6*(fc^4));

Whh = Evhh(1,1)*(0.99969+0.0144*fvhh-0.014364*(fvhh^2) +
      0.00042568*(fvhh^3)-5.58e-6*(fvhh^4));

Wlh = Evlh(1,1) * (0.99969+0.0144*fvlh-0.014364*(fvlh^2)+
      0.00042568*(fvlh^3)-5.58e-6*(fvlh^4));
```

```
***** C1-HH1 and C1-LH1 Transition Energies *****

E11h = EgInGaAs + Wc + Whh + DeltaEc + DeltaEhh
E11l = EgInGaAs + Wc + Wlh + DeltaEc + DeltaElh


E11hw = 1.24/E11h;
E11lw = 1.24/E11l;
```

APPENDIX C
CALCULATION OF THE REFRACTIVE INDICES
FOR THE LAYERS IN STRUCTURES S1 AND S2

Program to Calculate the Refractive Indices
Of the Different Layers in Structures S1 & S2

```
clc
clear
clg

m=zeros(4,1);
nGaAs = zeros(1,500);
nInGaAs = zeros(1,500);
Wavelength = zeros(1,500);
Energy1 = zeros(1,500);
Wavelength1 = zeros(1,500);


y=0.2;
EgAlGaAs=1.424+1.266*y+0.26*y^2;
EcAlGaAs=3.65+0.871*y+0.179*y^2;
EdAlGaAs=36.1-2.45*y;
```

```
x=0.1;
EgInGaAs=0.36+0.505*(1-x)+0.555*((1-x)^2);
EoInGaAs=3.65-2.15*x;
EdInGaAs=36.1-19.9*x;

EgGaAs=1.42;
EoGaAs=3.65;
EdGaAs=36.1;

i1=(EgAlGaAs+0.3)*500 + 1;
nAlGaAs = zeros(1,i1);
Energy1 = zeros(1,i1);
Wavelength1=zeros(1,i1);
t=1;

for E=0.2:0.002:EgAlGaAs+0.5
Energy1(1,t)=E;
Wavelength1(1,t)=1.24/E;
p=1+((E/EoAlGaAs)^2);
q=(E^4/(2*(EoAlGaAs^2)*((EoAlGaAs^2)-(EgAlGaAs^2))));
v=log((2*(EoAlGaAs^2)-(EgAlGaAs^2)-(E^2))/((EgAlGaAs^2)-
E^2));
nAlGaAs(1,t)=(1+(EdAlGaAs/EoAlGaAs)*(p+q*v))^0.5;
t=t+1;
end

i2=(EgInGaAs+0.3)*500 + 1;
```

```
nInGaAs = zeros(1,i2);
Energy2 = zeros(1,i2);
Wavelength2=zeros(1,i2);
t=1;
for E=0.2:0.002:EgInGaAs+0.5
Energy2(1,t)=E;
Wavelength2(1,t)=1.24/E;
p=1+((E/EoInGaAs)^2);
q=(E^4/(2*(EoInGaAs^2)*((EoInGaAs^2)-(EgInGaAs^2))));
v=log((2*(EoInGaAs^2)-(EgInGaAs^2)-(E^2))/((EgInGaAs^2)-
E^2));
nInGaAs(1,t)=(1+(EdInGaAs/EoInGaAs)*(p+q*v))^0.5;
t=t+1;
end
i3=(EgGaAs+0.3)*500 + 1;
nGaAs = zeros(1,i3);
Energy3 = zeros(1,i3);
Wavelength3=zeros(1,i3);
t=1;
for E=0.2:0.002:EgGaAs+1.5
p=1+((E/EoGaAs)^2);
q=(E^4/(2*(EoGaAs^2)*((EoGaAs^2)-(EgGaAs^2))));
v=log((2*(EoGaAs^2)-(EgGaAs^2)-(E^2))/((EgGaAs^2)-E^2));
nGaAs(1,t)=(1+(EdGaAs/EoGaAs)*(p+q*v))^0.5;
Energy3(1,t)=E;
Wavelength3(1,t)=1.24/E;
t=t+1;
```

```
end

***** Plots of Refractive Indices of *****
***** GaAs AlGaAs and InGaAs vs. Energy *****


m(1,1)=0.2;m(2,1)=1.6;m(3,1)=3.2;m(4,1)=3.8;

axis(m)

plot(Energy1(1,1:i1),nAlGaAs(1,1:i1),Energy2(1,1:i2),nInGaAs(

1,1:i2),'--',Energy3,nGaAs,'-.')

title('Refractive Index vs Energy')

xlabel('Energy(eV)')

ylabel('n(InGaAs-top,GaAs-middle,AlGaAs-bottom)')

grid

text(1,3.7,'InGaAs --')

text(1,3.65,'GaAs -.')

text(1,3.6,'AlGaAs -')
```

APPENDIX D
CONDITIONS FOR SINGLE MODE OPERATION

The following program uses the multilayer matrix method to find the propagation constants of the fundamental mode for the samples S1 and S2, making sure that the choice of layer thicknesses and compositions is suitable for single lateral mode operation. Furthermore, the mode field of these structures is plotted, showing how the optical field is distributed inside each structure. The refractive indices for the different layers are derived in Appendix C.

The last part of the program deals with the design of a single mode ridge waveguide, using the effective index method. If a certain waveguide width is needed, we consider the structure to be etched to a certain depth. Then we find the effective index in such structure. Using some iteration, the amount of etch (or the width of the waveguide) can be determined to insure single mode operation.

Program to Obtain the Propagation Constant &
Mode Field in Proposed Structures

```
clc

clg

clear

***** Values of the Refractive Indices & *****
*****  Thicknesses for Different Layers  *****


n1=1;

n2=3.53;h2=0.05;

n3=3.419;h3=1;

n4=3.438;h4=0.25;h41=0.2;

n5=3.4578;h5=0.25;

n6=3.438;h6=.25;

n7=3.419;

λ=0.9538;


***** Constants and Intialiazation of Variables *****


j=sqrt(-1);

A=0;

B=0;

C=0;

D=0;

E=0;

F=0;

G=0;
```

```
H=0;
I=0;
J=0;
e1=0;
W=0;
k0=2*pi/λ;
cnt2=0;z=0;
u1=(n5-n3-0.0002)*10000;
u=zeros(u1,1);
v=zeros(4,1);
x=zeros(5,1);
y=zeros(5,1);
cnt3=0;
cnt4=1;
o1=0;
o2=0;
o3=0;
o4=0;r=zeros(1,1);
s=0;
f1=zeros(u1,1);
f2=zeros(u1,1);

c=zeros(2,2);
m= zeros(2,2);
m2=zeros(2,2);
m3=zeros(2,2);
m4=zeros(2,2);
```

```
m41=zeros(2,2);
m5=zeros(2,2);
m6=zeros(2,2);
t=zeros(2,2);
cnt=2;

***** Multilayer Matrix Method *****

for N=n5-0.0001:-0.0001:n3+0.0001
u(cnt4,1)=N;
i2=n2^2-N^2;
i3=n3^2-N^2;
i4=n4^2-N^2;
i5=n5^2-N^2;
i6=n6^2-N^2;
ka2=k0*sqrt(abs(i2));
if i2<0
ka2=ka2*j;
end

ka3=k0*sqrt(abs(i3));

if i3<0
ka3=j*ka3;
end

ka4=k0*sqrt(abs(i4));
```

```
if i4<0
ka4=ka4*j;
end

ka5=k0*sqrt(abs(i5));

if i5<0
ka5=ka5*j;
end

ka6=k0*sqrt(abs(i6));

if i6<0
ka6=ka6*j;
end

m2(1,1)=cos(ka2*h2);
m3(1,1)=cos(ka3*h3);
m4(1,1)=cos(ka4*h4);
m41(1,1)=cos(ka4*h41);
m5(1,1)=cos(ka5*h5);
m6(1,1)=cos(ka6*h6);

m2(2,2)=m2(1,1);
m3(2,2)=m3(1,1);
m4(2,2)=m4(1,1);
```

```
m41(2,2)=m41(1,1);
m5(2,2)=m5(1,1);
m6(2,2)=m6(1,1);

m2(1,2)=(j*sin(ka2*h2))/ka2;
m2(2,1)=j*ka2*sin(ka2*h2);

m3(1,2)=(j*sin(ka3*h3))/ka3;
m3(2,1)=j*ka3*sin(ka3*h3);

m4(1,2)=(j*sin(ka4*h4))/ka4;
m4(2,1)=j*ka4*sin(ka4*h4);

m41(1,2)=(j*sin(ka4*h41))/ka4;
m41(2,1)=j*ka4*sin(ka4*h41);

m5(1,2)=(j*sin(ka5*h5))/ka5;
m5(2,1)=j*ka5*sin(ka5*h5);

m6(1,2)=(j*sin(ka6*h6))/ka6;
m6(2,1)=j*ka6*sin(ka6*h6);

m=m6*m5*m4*m3*m2;
t=m6*m5*m41;

m(1,2)=-m(1,2)*j;
m(2,1)=-m(2,1)*j;
```

```
t(1,2)=-t(1,2)*j;
t(2,1)=-t(2,1)*j;

gc=k0*sqrt(N^2-n1^2);
gs=k0*sqrt(N^2-n7^2);
f1(cnt-1,1)=atan((gs*m(1,1)+gc*m(2,2))-m(2,1)+gc*gs*m(1,2));
f2(cnt-1,1)=atan((gs*t(1,1)+gc*t(2,2))-t(2,1)+gc*gs*t(1,2));

if cnt>2
  o1=sign(f1(cnt-2,1));
o2=sign(f1(cnt-1,1));
if (o1+o2)==0
cnt2=cnt2+1;
x(cnt2)=N;
beta2=k0*N;
end
o3=sign(f2(cnt-2,1));
o4=sign(f2(cnt-1,1));

if (o3+o4)==0
cnt3=cnt3+1;
y(cnt3)=N;
beta1=k0*N;
end

cnt4=cnt4+1;
end
```

```
cnt=cnt+1;

end

***** Using the Effective Index Method to  *****
***** Calculate the Width of the Ridge Guide *****


cnt6=1;

for d=0.1:0.1:8

r(1,1)=k0*d*sqrt(x(1,1)^2-y(1,1)^2);

if r(1,1)>=pi & cnt6==1

s=d;

MaxWidth_μm=s

cnt6=cnt6+1;


end

end


W=round(MaxWidth_μm);

if W-MaxWidth_μm >0

W=W-1;

end

if abs(W-MaxWidth_μm)<1e-4

W=W-0.1;

end

W


***    Using the Multilayer Matrix Method to Determine ***
*** The Mode Field and Effective Index ***
*** of Etched Structure ***
```

```
cnt2=0;
u2=(x(1,1)-y(1,1)-0.0001)*100000;
f3=zeros(u2,1);
g=zeros(u2,1);
cnt=1;
for i=y(1,1):0.00001:x(1,1)-0.00001
cnt=cnt+1;
g(cnt-1,1)=i;
il=x(1,1)^2-i^2;
kl=k0*sqrt(abs(il));
c(1,1)=cos(kl*(W));
c(1,2)=(j*sin(kl*(W)))/kl;
c(2,2)=c(1,1);
c(2,1)=j*kl*sin(kl*(W));
c(1,2)=-c(1,2)*j;
c(2,1)=-c(2,1)*j;
gc=k0*sqrt(i^2-y(1,1)^2);
gs=k0*sqrt(i^2-y(1,1)^2);
f3(cnt-1,1)=atan((gs*c(1,1)+gc*c(2,2))-c(2,1)+gc*gs*c(1,2));

if cnt>2
o1=sign(f3(cnt-2,1));
o2=sign(f3(cnt-1,1));

if (o1+o2)==0
z=i;
end
```

```
end

end

E1=zeros((h2+h3+h4+h5+h6+4)*100+1,1);
E2=zeros((h41+h5+h6+4)*100+1,1);
E3=zeros(((W+4)*100)+1,1);

d1=zeros((h2+h3+h4+h5+h6+4)*100+1,1);
d2=zeros((h41+h5+h6+4)*100+1,1);
d3=zeros(((W+4)*100)+1,1);

theta1=asin(x(1,1)/n5);
theta2=asin(y(1,1)/n5);
theta3=asin(z/x(1,1));

Kappa1=k0*n5*cos(theta1);
Kappa2=k0*n5*cos(theta2);
Kappa3=k0*x(1,1)*cos(theta3);

Ga11=k0*sqrt(x(1,1)^2-n1^2);
Ga12=k0*sqrt(x(1,1)^2-n2^2);
Ga13=k0*sqrt(x(1,1)^2-n3^2);
Ga14=k0*sqrt(x(1,1)^2-n4^2);
Ga16=k0*sqrt(x(1,1)^2-n6^2);
Ga17=k0*sqrt(x(1,1)^2-n7^2);
```

```
Ga21=k0*sqrt(y(1,1)^2-n1^2);
Ga24=k0*sqrt(y(1,1)^2-n4^2);
Ga26=k0*sqrt(y(1,1)^2-n6^2);
Ga27=k0*sqrt(y(1,1)^2-n7^2);

Gamma3=k0*sqrt((x(1,1)*sin(theta3))^2-y(1,1)^2);

A=((0.5*cos(Kappa1*(h5/2)))+(Kappa1*0.5*sin(Kappa1*(h5/2))/Ga
14));
B=((0.5*cos(Kappa1*(h5/2)))-
(Kappa1*0.5*sin(Kappa1*(h5/2))/Ga14));
D=0.5*(A*exp(-Ga14*h4)+B*exp(Ga14*h4))+ (0.5*Ga14/Ga13)*(-
A*exp(-Ga14*h4)+B*exp(Ga14*h4));
C=-D+(A*exp(-Ga14*h4)+B*exp(Ga14*h4));
F=0.5*(C*exp(-Ga13*h3)+D*exp(Ga13*h3))+ (0.5*Ga13/Ga12)*(-
C*exp(-Ga13*h3)+D*exp(Ga13*h3));
E=-F+(C*exp(-Ga13*h3)+D*exp(Ga13*h3));
G=E*exp(-Ga12*h2)+F*exp(Ga12*h2);
I=((0.5*cos(Kappa1*(h5/2)))+(Kappa1*0.5*sin(Kappa1*(h5/2))/Ga
16));
H=((0.5*cos(Kappa1*(h5/2)))-
(Kappa1*0.5*sin(Kappa1*(h5/2))/Ga16));
J=H*exp(Ga16*h6)+I*exp(-Ga16*h6);

A1=((0.5*cos(Kappa2*(h5/2)))+(Kappa2*0.5*sin(Kappa2*(h5/2))/G
a24);
```

```
B1=((0.5*cos(Kappa2*(h5/2)))-
(Kappa2*0.5*sin(Kappa2*(h5/2))/Ga24))
I1=((0.5*cos(Kappa2*(h5/2)))+(Kappa2*0.5*sin(Kappa2*(h5/2))/G
a26))
H1=((0.5*cos(Kappa2*(h5/2)))-
(Kappa2*0.5*sin(Kappa2*(h5/2))/Ga26))
J1=H1*exp(Ga26*h6)+I1*exp(-Ga26*h6);
G1=A1*exp(-Ga24*h41)+B1*exp(Ga24*h41);

M=1;
for i=-2-h6:0.01:h5+h4+h3+h2+2
d1(M,1)=i;

if i>=0 & i<=h5
E1(M,1)=cos(Kappa1*(i-(h5/2)));
end

if i>h5 & i<= h5+h4
E1(M,1)=A*exp(-Ga14*(i-h5))+B*exp(Ga14*(i-h5));
end

if i>h5+h4 & i<=h3+h4+h5
E1(M,1)=C*exp(-Ga13*(i-h5-h4))+D*exp(Ga13*(i-h5-h4));
end


if i>h3+h4+h5 & i<= h2+h3+h4+h5
```

```
E1(M,1)=E*exp(-Ga12*(i-h5-h4-h3)) + F*exp(Ga12*(i-h5-h4-h3));
end

if i>h2+h3+h4+h5
E1(M,1)=G*exp(-Ga11*(i-h2-h3-h4-h5));
end

if i<0 & i>=-h6
E1(M,1)=I*exp(Ga16*i)+H*exp(-Ga16*i);
end

if i<-h6
E1(M,1)=J*exp(Ga17*(i+h6));
end
M=M+1;
end

M=1;
for i=h41+2:-0.01:-h5-h6-2
d2(M,1)=i;
if i<0 & i>=-h6
E2(M,1)=I1*exp(Ga26*i)+H1*exp(-Ga26*i);
end

if i<-h6
E2(M,1)=J1*exp(Ga27*(i+h6));
end
```

```
if i>=0 & i<=h5
E2(M,1)=cos(Kappa2*(i-(h5/2)));
end

if i>h5 & i<= h5+h41
E2(M,1)=A1*exp(-Ga24*(i-h5))+B1*exp(Ga24*(i-h5));
end

if i>h41+h5
E2(M,1)=G1*exp(-Ga21*(i-h41-h5));
end
M=M+1;
end
M=1;
for i=2+W:-0.01:-2
d3(M,1)=i;
if i>=0 & i<=W
E3(M,1)=cos(Kappa3*(i-(W/2)));
end
if i>W
E3(M,1)=cos(Kappa3*W/2)*exp(-Gamma3*(i-W));
end
if i<0
E3(M,1)=cos(Kappa3*W/2)*exp(Gamma3*i);
end
M=M+1;
```

```
end


*****  Graphs of Effective Indices of the Whole,   *****
*****  The Etched and the Three-Layer Structures   *****


v(1,1)=n3;v(2,1)=n5;v(3,1)=-2;v(4,1)=2;

axis(v)

subplot(221)

plot(u,f1(1:u1,1))

title('Effective Index for the Whole Structure')

xlabel('Refractive Index')

grid

subplot(222)

plot(u,f2(1:u1,1))

title('Effective Index for the Etched Structure')

xlabel('Refractive Index')

grid

v(1,1)=y(1,1);v(2,1)=x(1,1);v(3,1)=-2;v(4,1)=2;

axis(v)

subplot(223)

plot(g,f3)

title('Effective Index for the Three-layer Structure')

xlabel('Refractive Index')

grid

pause

clg
```

```
***** Mode Fields in All Three Structures *****

v(1,1)=-h6-2;v(2,1)=h5+h4+h3+h2+2;v(3,1)=0;v(4,1)=1.5;
axis(v)
subplot(221)
plot(d1,E1)
title('Mode Field in Complete Structure')
xlabel('Distance (μm)')
grid

v(1,1)=-h6-2;v(2,1)=h5+h41+2;v(3,1)=0;v(4,1)=1.5;
axis(v)
subplot(222)
plot(d2,E2)
title('Mode Field in Etched Structure')
xlabel('Distance (μm)')
grid

v(1,1)=-W;v(2,1)=2*W;v(3,1)=0;v(4,1)=1.5;
axis(v)
subplot(223)
plot(d3,E3)
title('Mode Field in Ridge Waveguide')
xlabel('Distance (μm)')
grid
```

REFERENCE LIST

[1] P. L. Gowley, and L. R. Dawson, J. Appl. Phys., **65**, pp.380 (1989).

[2] P. D. Hudson, R. H. Wallis, and J. I. Davies, IEE Proc., Part J, Optoelectronics, **135**, pp. 2 (1989).

[3] R. Grey, J. P. R. David, P. A. Glaxton, J. Appl. Phys., **66**, pp.975 (1989).

[4] D.J. Arent, K. Deneffe, and C. Van Hoof, J. Appl. Phys., **66**, pp. 1739 (1989).

[5] V. A. Wilkins, A. D. Prins, and D.J. Dunston, J. Elect. Mat., **20**, pp.509 (1991).

[6] D. L. Smith, Solid State Communications, **57**, pp. 919 (1986).

[7] D. L. Smith and C. Mailhiot, Rev. Mod. Phys., **62**, pp. 173 (1990).

[8] B. K. Laurich, K. Elcess, C. G. Fonstad, J. G. Beery, C. Mailhiot, and D. L. Smith, Phys. Rev. Lett., **67**, pp.649 (1989).

[9] E. A. Caridi, T. Y. chang. K. W. Goossen, and L. F. Eastman, Appl. Phys. Lett, **56**, pp. 659 (1990).

[10] K. W. Goossen, E. A. Caridi, T. Y. Chang, J. B. Stark, and D. A. B. Miller, Appl. Phys. Lett., **56**, pp. 715 (1990).

[11] D. A. B. Miller, D. S. Chemla, T. C. Damen, A. C. Gossard, W. Wiegmann, T. H. Wood, and C. A. Burrus. Physical Review B, **32**, pp. 1043 (1985).

[12] T. Hayakawa, M. Kondo, T. Suyamaa, K. Takahashi, S. Yamamoto, and T. Hijikata, Jpn. J. Appl. Phys., **26**, L302 (1987).

[13] A. Chin, T. Y. Chang, A. Ourmazd, and E. M. Monberg, Appl. Phys. Lett., **58**, pp. 968 (1991).

[14] D.L. Smith and C. Mailhiot, Phys. Rev. Lett., **58**, p. 1264 (1987).

[15] A. Y. Cho, J. Appl. Phys., **41**, p. 2780 (1970).

[16] A. Chin, P. Martin, P. Ho, J. Ballingall, T. H. Yu, and J. Mazurowski, Appl. Phys. Lett., **59**, p. 1899 (1991).

[17] A. Chin, P. Martin, J. Ballingall, T. H. Yu, and J. Mazurowski, Appl. Phys. Lett., **59**, p. 2394 (1991).

[18] A. Chin, T. M. Cheng, S. P. Peng, Z. Osman, U. Das, C. Y. Chang, Appl. Phys. Lett., **63**, p. 2381 (1993).

[19] M. A. Herman and H. Sitter, Molecular Beam Epitaxy Fundamentals and Current Status (Springer-Verlag, Berlin 1989).

[20] M. A. Herman, Vacuum, **32**, p. 555 (1982).

[21] E. H. C. Parker, The Technology and Physics of Molecular Beam Epitaxy (Plenum, New York, 1985).

[22] A. Madhukar, Surface Science, **132**, p. 344 (1983).

[23] M. A. Herman, Semiconductor Superlattices (Akademie-Verlag, Berlin 1986).

[24] F. Bechstedt and R. Enderlein, Semiconductor Surfaces and Interfaces (Akademie-Verlag, Berlin 1988).

[25] K. Nishi and T. Anan, Journal of Applied Physics, **70**, p. 5004 (1991).

[26] T. Hayakawa, K. Takahashi, M. Kondo, T. Suyama, S. Yamanoto and T. Hijikata, Phys. Rev. Lett., **60**, p. 349 (1988).

[27] B.V. Shanabrook, O.J. Glembocki, D.A. Broido, L. Vina and W.I. Wang, Journal de Physique, **C5**, Supplement #11, p. 235 (1987).

[28] J. M. Luttinger, Phys. Rev., **102**, p. 1030 (1956).

[29] P. Lawatez, Phys. Rev. B, **4**, p. 3460 (1971).

[30] J.F. Nye, Physical Properties of Crystals (Oxford University, Amen House, London, 1964).

[31] W.F. Cady, Piezoelectricity (McGraw-Hill, New York, 1946).

[32] J. H. van der Merve, Journal of Applied Physics, **34**, p. 117 (1963).

[33] G.H. Olsen, C.J. Nuese, and R.T. Smith, Journal of Applied Physics, **49**, p.5523 (1978).

[34] S. de Gironcoli, S. Baroni, and R. Resta, Phys. Rev. Lett., **62**, p. 2853 (1989).

[35] P. Arlt and P.Q. Quadflieg, Phys. Status Solidi, **25**, p. 323 (1968).

[36] J. W. Matthews, and A. E. Blakeslee, J. Cryst. Growth, **27**, p. 118 (1974).

[37] D. Morris, A. P. Roth, R.A. Masut, C. Lacelle, and J. L. Brebner, J. Appl. Phys., **64**, p. 4135 (1988).

[38] Takayoshi Anan, Kenichi Nishi, and Siego Sugou, Appl. Phys. Lett., 60, p. 315 (1992).

[39] R. de Laer Kronig, and W. J. Penney, Proc. Roy. Soc. London, **A130**, p. 499 (1930).

[40] M. Shur, Physics of Semiconductor Devices (Prentice Hall,Englewood Cliffs, New Jersey, 1990).

[41] H. Asai and K. Oe, J. Appl. Phys., **54**, p. 2052 (1983).

[42] Y. Kajikawa, N. Sugiyama, T. Kamijoh and Y. Katayama, Jpn. J. Appl. Phys., **28**, p. L1022 (1989).

[43] L. O. Landau and E. M. Lifshitz, Quantum Mechanics Non-Relativistic Theory (Pergamon, New York, 1981).

[44] A. Rabinowitch and J. Zak, Phys. Rev. B, **4**, p. 2358 (1971).

[45] T. Lukes and G. A. Ringwood, Physica, **84A**, p. 421 (1976).

[46] M. Abramowitz and I. A. Stegun, Handbook of Mathematical Functions (National Bureau of Standards, Washington D.C., 1964).

[47] K. W. Goossen, E. A. Caridi, T. Y. Chang, J. B. Stark, and D. A. B. Miller, Appl. Phys. Lett., **56**, p. 715 (1990).

[48] H. Shen, M. dutta, W. Chang, R. Moerkirk, D. M. Kim, K. W. Chung, P. P. Ruden, M. I. Nathan, and M. A. Strscio, Appl. Phys. Lett., **60**, p. 2400 (1992).

[49] T.S. Moise, L. J. Guido, R. C. Barker, J. O. White, and A. R. Kost, Appl. Phys. Lett., **60**, p. 2637 (1992).

[50] B. E. A. Saleh, M. C. Teich, Fundementals of Photonics (Wiley-Interscience, New York 1991).

[51] J. Verdeyen, Laser Electronics (Prentice Hall,Englewood Cliffs, New Jersey, 2nd edition, 1989).

[52] Jacques I. Pankove, Optical Processes in Semiconductors (Dover, New York 1971).

[53] Utpal Das, Yi Chen, and Bhattacharya, Appl. Phys. Lett., **51**, p. 1679 (1987).

[54] C. Thistrup, P. Li Kam Wa, M. A. Pate, J. S. Roberts, and P. N. Robson, Electronics Letters, **25**, p. 1668 (1989).

[55] P. Li Kam Wa, J.E. Sitch, M.J. Mason, J.S. Roberts, and P. N. Robson, Electronics Letters, **21**, p. 26 (1985).

[56] M. Born, and E. Wolf, Principles of Optics (Pergamon, New York, 1959).

[57] F. Abeles, Ann. Physique, **5**, p. 596 (1950).

[58] S. H. Wemple, and M. DiDomenico Jr., Phys. Rev., **B3**, p. 1338 (1971).

[59] M. A. Afromowitz, Solid State Communication, **15**, p. 59 (1974).

[60] R. E. Nahory, M. A. Pollack, W. D. Johnston, and R. L. Barns, Appl. Phys. Lett., **33**, p. 660 (1978).

[61] K. Utaka, Y. Suematsu, K. Kobayashi, and H. Kawanishi, Jpn. J. Appl. Phys., **19**, p. L137 (1980).

[62] B. Broberg and S. Lindgren, J. Appl. Phys., **55**, p. 3376 (1984).

[63] U. Das, and P. K. Battacharya, J. Appl. Phys., **58**, p. 341, 1985.

[64] M. Glick and F. K. Reinhart, Helvetica Physica Acta, **58**, p.403 (1985).

[65] A. Yariv, Quantum Electronics (Wiley, New York, 3rd edition 1989).

[66] A. S. Pabla, J. L. Sanchez-Rojas, J. Woodhead, R. Grey, J. P. R. David, G. J.Rees, G. Hill, M. A. Pate, P. N. Robson, R. A. Hogg, T. A. Fisher, A. R. K.Wilcox, D. M.

Whittaker, M. S. Skolnick, and D. J. Mowbray, Appl. Phys. Lett., **63**, p. 752 (1993).

[67] T. S. Moise, L. J. Guido, J. C. Beggy, T. J. Cunningham, S. Seshadri, and R. C. Barker, J. Elect. Mat., **21**, p. 119 (1992).

[68] M. Sheik-Bahae, D. C. Hutchings, D. J. Hagan, and E. W. Van Stryland, IEEE J. Quant. Elect., **27**, p. 1296, 1991.

BIOGRAPHICAL SKETCH

Ziad Ahmad Osman was born on January 18th, 1965, in Beirut, Lebanon, which is a small country laying off the eastern shore of the Mediterranean sea. He grew up there and graduated from Bir-Wil Ehssan High School in 1982. He then enrolled at the Beirut Arab University and graduated with honors in September of 1987, with a Bachelor of Science degree in electrical engineering. After graduation he spent a year working as a teaching assistant at the above mentioned university. Then, in January of 1989, he came to the University of Florida where he was enrolled in the master's program. He has been involved in research in photonics since August 1989. Upon completion of the M.E. degree, he continued his studies to obtain a Ph.D. degree.

After graduation, Dr. Osman is planning to pursue a career in the design and characterization of semiconductor based optical devices.

I certify that I have read this study and that in my opinion it conforms to acceptable standards of scholarly presentation and is fully adequate, in scope and quality, as a dissertation for the degree of Doctor of Philosophy.

Ramakant Srivastava, Chairman
Professor of Electrical Engineering

I certify that I have read this study and that in my opinion it conforms to acceptable standards of scholarly presentation and is fully adequate, in scope and quality, as a dissertation for the degree of Doctor of Philosophy.

Utpal Das, Cochairman
Assistant Professor of Electrical Engineering

I certify that I have read this study and that in my opinion it conforms to acceptable standards of scholarly presentation and is fully adequate, in scope and quality, as a dissertation for the degree of Doctor of Philosophy.

Peter Zory
Professor of Electrical Engineering

I certify that I have read this study and that in my opinion it conforms to acceptable standards of scholarly presentation and is fully adequate, in scope and quality, as a dissertation for the degree of Doctor of Philosophy.

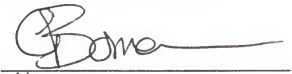

Gijs Bosman
Professor of Electrical Engineering

I certify that I have read this study and that in my opinion it conforms to acceptable standards of scholarly presentation and is fully adequate, in scope and quality, as a dissertation for the degree of Doctor of Philosophy.

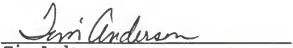

Tim Anderson
Professor of Chemical Engineering

This dissertation was submitted to the Graduate Faculty of the College of Engineering and to the Graduate School and was accepted as partial fulfillment of the requirements for the degree of Doctor of Philosophy.

August 1994

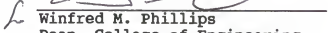

Winfred M. Phillips
Dean, College of Engineering

Karen A. Holbrook
Dean, Graduate School